

Stability and dynamics of the flow past a bullet-shaped blunt body moving in a pipe

Paul Bonnefis¹, David Fabre^{1,†} and Christophe Airiau¹

¹IMFT, Université de Toulouse, UMR 5502 CNRS / INPT / UPS, Allée du Pr Camille Soula, 31400 Toulouse, France

(Received 17 December 2021; revised 20 April 2022; accepted 6 June 2022)

The flow past a bullet-shaped blunt body moving in a pipe is investigated through global linear stability analysis (LSA) and direct numerical simulation. A cartography of the bifurcation curves is provided thanks to LSA, covering the range of parameters corresponding to Reynolds number $Re = [50-110]$, confinement ratio $a/A = [0.01-0.92]$ and length-to-diameter ratio $L/d = [2-10]$. Results show that the first bifurcation is always a steady bifurcation associated to a non-oscillating eigenmode with azimuthal wavenumber $m = \pm 1$ leading to a steady state with planar symmetry. For weakly confined cases ($a/A < 0.6$), the second bifurcation is associated to an oscillating mode with azimuthal wavenumber $m = \pm 1$, as in the unconfined case. On the other hand, for the strongly confined case ($a/A > 0.8$), a destabilization of non-oscillating modes with $|m| = 2, 3$ and a restabilization of the $m = \pm 1$ eigenmodes are observed. The aspect ratio L/d is shown to have a minor influence for weakly confined cases and almost no influence for strongly confined cases. Direct numerical simulation is subsequently used to characterize the nonlinear dynamics. The results confirm the steady bifurcation predicted by LSA with excellent agreement for the threshold Reynolds. For weakly confined cases, the second bifurcation is a Hopf bifurcation leading to a periodic, planar-symmetric state in qualitative accordance with LSA predictions. For more confined cases, more complex dynamics is obtained, including a steady state with $|m| = 3$ geometry and aperiodic states.

Key words: wakes

1. Introduction

The flow past blunt bodies is a problem of practical importance, with obvious engineering applications to transport. In such applications it is necessary to estimate and predict the

† Email address for correspondence: david.fabre@imft.fr

lift and drag forces exerted on the body as well as to assert the influence of the geometry on these forces for a shape optimization procedure. Wake flows in the transitional regime (with Reynolds numbers of order 10^2 – 10^3) is also a problem of fundamental interest where global stability theory and bifurcation theory have been particularly successful to explain complex nonlinear dynamics. The most documented case corresponds to the wake of a cylindrical body placed perpendicularly to the flow (Bénard 1908; Von Kármán 1912; Provansal, Mathis & Boyer 1987). This case is characterised by a Hopf bifurcation for $Re \approx 47$ giving rise to the well-known Bénard–Von Kármán vortex street. Secondary bifurcations occurring in the range $Re \approx 200$ and leading to three-dimensional states have also been investigated by stability analysis of the periodic solution and bifurcation theory (Thompson, Hourigan & Sheridan 1996). Among three-dimensional geometries, spheres and disks have been particularly considered as canonical cases. Linear stability analysis (LSA) (Natarajan & Acrivos 1993; Meliga, Chomaz & Sipp 2009a) provides a powerful framework allowing us to tackle this class of problems. This approach predicts that the first unstable mode is a non-oscillating mode (i.e. with a purely real global eigenvalue) characterised by azimuthal wavenumbers $m = \pm 1$. It leads to a steady state solution with planar symmetry, the presence of a pair of longitudinal vortices and finally a non-zero lift force exerted on the body. The LSA study also predicts the onset of a secondary eigenmode which is oscillating (i.e. a pair of complex conjugated eigenvalues) and also associated to an azimuthal wavenumber $m = 1$. Comparisons with direct numerical simulations (DNS) and application of normal form theory (Fabre, Auguste & Magnaudet 2008; Auguste, Fabre & Magnaudet 2010) and weakly nonlinear analysis (Meliga *et al.* 2009a) showed that this secondary mode is responsible for the onset of an oscillating state which is either reflection-symmetry preserving (RSP) for spheres and thick disks or reflection-symmetry breaking for thin disks. Effects of motion of the body have also been considered. First, the effect of imposed rotation on the wake of a sphere has been analysed. In the case the axis of rotation is aligned with the flow, rotation breaks the symmetry between $m = +1$ and $m = -1$ modes and modifies the bifurcation scenario leading to the onset of quasi-periodic states (Pier 2013). In the case the axis is transverse, weak rotation stabilizes the RSP mode but strong rotation gives rise to a new oscillating mode with a smaller frequency (Citro *et al.* 2016; Fabre *et al.* 2017). Secondly, Tchoufag, Fabre & Magnaudet (2014) have demonstrated the influence of wake dynamics on the motion of bodies in free movement submitted to a buoyancy force. In that case, the destabilization of the base flow field may result in a path deviation of the buoyancy-driven disk or sphere leading to a variety of states including zig-zag paths, steady-oblique paths, etc.

Another canonical blunt body geometry which was selected by a number of studies in the literature is the bullet-shaped body, consisting of a half-ellipsoidal nose glued to a cylindrical blunt rear. It has the advantage of having a shape closer to real industrial applications such as trains for instance. Experiments performed by Brücker (2001) revealed a stabilizing effect of the presence of the ellipsoidal nose, in comparison with the flow past disks. An extensive study presented by Bohorquez *et al.* (2011) uses three approaches, DNS, LSA and experiments. This study reveals that the bifurcation sequences and wake patterns are globally similar to the case of a sphere, and that increasing the length of the body generally delays the bifurcations towards larger Reynolds numbers. A base-bleed flow control has also been tested and its stabilizing effect was demonstrated. The sequence of bifurcations occurring in the wake has been examined by Bury & Jardin (2012) using DNS, from the laminar axisymmetric wake to the onset of chaotic behaviour. In Jiménez-González *et al.* (2014) the effect of spinning this blunt body around its axis of symmetry is shown to have a stabilizing effect, promoting the second most amplified

Flow past a bullet-shaped blunt body in a pipe

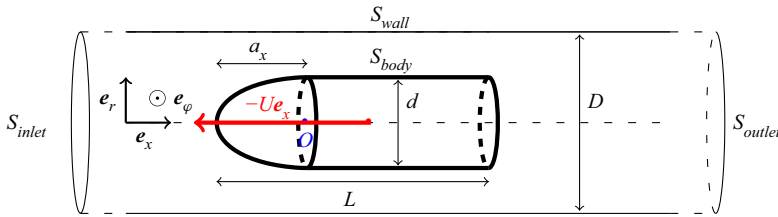


Figure 1. Geometry of the axisymmetric blunt body in a pipe.

mode and widening the range of existence of a stable axisymmetric wake. Note that a series of recent works have also been conducted for the wake of axisymmetric bodies for much larger ranges of Reynolds number and using a mean-flow based approach (Rigas *et al.* 2014, 2015; Rigas, Morgans & Morrison 2017; Callaham *et al.* 2021), indicating that linear stability and low-order nonlinear modelling is also relevant in this range.

The present study investigates the effect of confinement on wake dynamics. The effect of confinement on axisymmetric wakes has already been analysed from a fundamental point of view by Juniper (2006), who considered local stability analysis of a family of parallel flow models. Here we focus on the bullet-shaped blunt body (cf. figure 1), a canonical geometry which can help address many industrial issues experienced in the case of an object travelling in a confined environment. A good example is a high-speed train passing through a tunnel, how it enters the tunnel and how the tunnel influences the aerodynamics of the train (Baron, Mossi & Sibilla 2001; Mok & Yoo 2001; Kwon *et al.* 2003). The issue encountered relies more on the pressure wave created by the train nose and its interaction with the tunnel than the wake itself, but the drag is still of interest. In another study Choi & Kim (2014) investigated the optimization of the nose shape of the high-speed Korean subway and the tunnel cross-sectional area influence on the total drag. Of course, with velocities of several hundred kilometres per hour, the Reynolds numbers are of order 10^8 and characterisation of nonlinear dynamics in the transitional range may be irrelevant. The situation changes considering new technologies in train transportation such as an evacuated tube transportation system where a capsule travels at high velocity in a near vacuum network of pipes. Numerous studies describe the limitations and opportunities arising in such configurations (Braun, Sousa & Pekardan 2017; Opgenoord & Caplan 2018; Oh *et al.* 2019) and highlight differences in aerodynamics compared with standard trains. The expected operating pressure for such a system is in the range 1–100 Pa, leading to Reynolds numbers in the range 10^3 – 10^5 . Hence, characterisation of dynamics in the transitional range using a combination of LSA, bifurcation theory and DNS may be relevant. The identification of non-axisymmetric bifurcations giving rise to a lift force may be of practical interest in the operation of such devices. Such applications also operate in the transonic regime so that, for an accurate modelling, compressibility and rarefied gas effects should also be taken into account. However, as a first approach towards these problems, it might be interesting to stick to an incompressible flow and target the effect of confinement regardless of additional effects. Our current investigations on a slender axisymmetric blunt-based body moving in a tube is inspired by such industrial applications. In order to pave the way to such complicated problems, the study has been limited to incompressible flows and to a Reynolds number Re lower than 1500.

The paper is organized as follows. The configuration, the governing equations and the LSA equations and resolution methods are presented in § 2. Section 3 is devoted to the characterisation of instability properties thanks to LSA. A parametric study of

the linearly unstable modes is obtained as a function of the confinement ratio, of the length-to-diameter ratio and of the Reynolds numbers. Section 4 is dedicated to DNS and to comparisons with the results of the LSA analysis. Direct numerical simulation is used to confirm the predictions of LSA regarding the first bifurcation threshold and to explore the nonlinear behaviour arising away from this threshold. The paper ends with some concluding remarks. Two appendices have been added, the first one is the analytical solution of the annular Couette–Poiseuille flow and the last one is the mesh convergence study.

2. Methodology

2.1. Configuration and parameters

The geometry of the bullet-shaped blunt body moving in a tube and the main geometrical parameters are shown in figure 1. The body consists of a half-ellipsoid nose glued to a cylindrical rear. The diameter of the cylinder is referred to as d . The ellipsoid of revolution is defined by its major axis with $a_x = 2a_y = d$ and its minor axis which fits with the cylindrical section by imposing $a_y = a_z = d/2$.

The diameter of the pipe is noted as D , so that the effect of confinement will be defined by either a diameter ratio $\xi = d/D$ or an area ratio $a/A = \xi^2$, with $a = \pi d^2/4$ the frontal area of the body and $A = \pi D^2/4$ the area of the tube.

The origin of the frame is taken at the junction between half-spheroidal and cylindrical parts, so that the body spans from $x = -d$ (nose) to $x = L - d$ (base).

The object moves with a velocity U in the direction $-e_x$ and the wall of the pipe is fixed. Assuming the flow is incompressible and isothermal, the non-dimensional parameters of this problem are the Reynolds number $Re = \rho Ud/\mu$, the diameter aspect ratio $\xi = d/D$ and the length aspect ratio L/d . Here ρ and μ are respectively the constant density and dynamic viscosity of the fluid. In most cases the parameter L/d will be set to 2, except in §3.3 where the effect of this parameter will be investigated.

The study will be conducted in the frame of reference associated to the body. The boundaries of the computational domain are given in figure 1. It is limited by, respectively, an inlet section S_{inlet} and an outlet section S_{outlet} . In this frame, the body is fixed, and placed within an incoming flow U of direction $+e_x$ and the tube wall also moves at the same velocity with respect to the body. Hence, the dimensionless incompressible Navier–Stokes equations and associated boundary conditions are

$$\partial_t \mathbf{u} = \mathcal{NS}([\mathbf{u}, p]) \equiv -\mathbf{u} \cdot \nabla \mathbf{u} - \nabla p + \frac{2}{Re} \nabla \cdot \mathbf{D}(\mathbf{u}), \tag{2.1a}$$

$$\nabla \cdot \mathbf{u} = 0, \tag{2.1b}$$

$$\mathbf{u}|_{S_{body}} = \mathbf{0}, \tag{2.1c}$$

$$\mathbf{u}|_{S_{inlet} \cup S_{wall}} = e_x, \tag{2.1d}$$

$$\left[-pe_x + \frac{2}{Re} \mathbf{D}(\mathbf{u}) \cdot e_x \right]_{S_{outlet}} = \mathbf{0}, \tag{2.1e}$$

where \mathbf{u} is the relative velocity, and $\mathbf{D}(\mathbf{u}) = (\nabla \mathbf{u} + \nabla^T \mathbf{u})/2$ is the rate-of-strain tensor. The divergence formulation for the viscous terms is related to the choice of the finite element method (FEM) to solve the equations.

The governing equations are non-dimensionalized by the body velocity U , the fluid density ρ and the body diameter d . The last boundary condition is written as a no-stress condition on the outlet section, which is a convenient choice for an outlet condition with the FEM approach.

2.2. Global LSA

2.2.1. Equations

The global linear stability approach is performed in the line of the now classical approach described, for instance, in Sipp & Lebedev (2007), Fabre *et al.* (2018). Within the LSA framework, the velocity and pressure are decomposed into a base flow and a small perturbation as

$$\mathbf{u}(r, \varphi, x, t) = \mathbf{u}_b(r, x) + \epsilon \hat{\mathbf{u}}(r, x) e^{im\varphi + \lambda t}, \quad p(r, \varphi, x, t) = p_b(r, x) + \epsilon \hat{p}(r, x) e^{im\varphi + \lambda t}. \quad (2.2a,b)$$

Here $[\mathbf{u}_b; p_b]$ is the so-called ‘base flow’, namely the solution of the axisymmetric, time-independent version of (2.1),

$$\mathcal{NS}([\mathbf{u}_b, p_b]) = \mathbf{0}; \quad \nabla \cdot \mathbf{u}_b = 0. \quad (2.3a,b)$$

In (2.2a,b) a small-amplitude perturbation of the base flow is assumed in the form of an eigenmode $[\hat{\mathbf{u}}, \hat{p}]$ associated to an eigenvalue $\lambda = \lambda_r + i\lambda_i$. The real part of the eigenvalue is the growth rate. A positive value indicates here an amplification. The imaginary part is a non-dimensional frequency (time oscillation), which is most conveniently represented by the Strouhal number $St = \lambda_i/(2\pi)$ thanks to the non-dimensionalization choices. Fourier decomposition in the azimuthal direction is possible with the axisymmetric invariance and an azimuthal wavenumber $m \in \mathbb{Z}$ can be added in the exponential wave-like part of the perturbation. Introducing the decomposition (2.2a,b) into the Navier–Stokes equations and linearizing leads to an eigenvalue problem written as

$$\lambda \hat{\mathbf{u}} = \mathcal{LN}\mathcal{S}_{\mathbf{u}_b}([\hat{\mathbf{u}}, \hat{p}]), \quad (2.4a)$$

$$\nabla_m \cdot \hat{\mathbf{u}} = 0, \quad (2.4b)$$

$$\hat{\mathbf{u}}|_{S_{inlet} \cup S_{wall} \cup S_{body}} = \mathbf{0}, \quad (2.4c)$$

where $\mathcal{LN}\mathcal{S}^m$ is the linearized Navier–Stokes operator defined as

$$\mathcal{LN}\mathcal{S}_{\mathbf{u}_b}^m([\hat{\mathbf{u}}, \hat{p}]) = -\mathbf{u}_b \cdot \nabla_m \hat{\mathbf{u}} - \hat{\mathbf{u}} \cdot \nabla_m \mathbf{u}_b - \nabla_m \hat{p} + \frac{2}{Re} \nabla_m \cdot \mathbf{D}_m(\hat{\mathbf{u}}). \quad (2.5)$$

Here quantities ∇_m and \mathbf{D}_m are the gradient and rate-of-strain operators with $\partial_\varphi(\cdot)$ replaced by $i \times m(\cdot)$.

2.2.2. Resolution methods

The resolution methods employed here are essentially similar to those used in recent papers such as Tchoufag *et al.* (2014), Fabre *et al.* (2019), in which stability analysis of axisymmetric incompressible flows were considered.

Thanks to axisymmetry, the base flow velocity is searched in the cylindrical frame $[\mathbf{e}_x, \mathbf{e}_r, \mathbf{e}_\varphi]$ as $\mathbf{u}_b = [u_{b,x}(x, r), u_{b,r}(x, r), 0]$ so that only two components of velocity are kept. On the other hand, for eigenmodes, three components of velocity are needed, i.e. $\hat{\mathbf{u}} = [\hat{u}_x(x, r), \hat{u}_r(x, r), \hat{u}_\varphi(x, r)]$. Within this assumption it is enough to consider a two-dimensional numerical domain (Ω) corresponding to a meridian plane (x, r) .

For both base flow equations and linear stability equations, a FEM is used. For this sake, the equations are first turned into a weak form by introducing test functions \mathbf{v} and q and a scalar product $\langle \varphi_1, \varphi_2 \rangle = \int_{\Omega} \overline{\varphi_1} \cdot \varphi_2 \, d\Omega$. For instance, the weak form of the base flow (2.5) is written as

$$\forall(\mathbf{v}, q), \quad \langle \mathbf{v}, \mathcal{NS}([\widehat{\mathbf{u}}_b, \widehat{p}]) \rangle + \langle q, \nabla_0 \cdot \widehat{\mathbf{u}}_b \rangle = 0. \quad (2.6)$$

An integration by parts of the viscous terms is afterward performed and their derivation order is reduced. Dirichlet boundary conditions are incorporated by penalization while the stress-free outlet condition is directly satisfied thanks to integration by parts. The nonlinear problem is then solved using an iterative Newton method. The developed form of the base flow equations in cylindrical coordinates and details about the Newton method can be found, for instance, in Tchoufag *et al.* (2014), Fabre *et al.* (2019).

Similarly, the weak form of stability problem yields

$$\forall(\mathbf{v}, q), \quad \lambda \langle \mathbf{v}, \widehat{\mathbf{u}} \rangle = \langle \mathbf{v}, \mathcal{LN}S_{ub}^m([\widehat{\mathbf{u}}, \widehat{p}]) \rangle + \langle q, \nabla_m \cdot \widehat{\mathbf{u}} \rangle, \quad (2.7)$$

which after discretization leads to a generalized eigenvalue problem,

$$\lambda B \widehat{X} = A \widehat{X}. \quad (2.8)$$

A shift-and-invert method is applied to obtain a collection of eigenvalues (typically 10) located closest to a ‘shift’ value taken as a guess of the searched eigenvalues. As usual in such approaches, several values of the ‘shift’ were systematically tested to explore the complex plane and to ensure that no unstable eigenvalue was missed in the study.

The weak form of the stability equations, details about the integration by parts and the construction of matrices A and B can again be found in Tchoufag *et al.* (2014), Fabre *et al.* (2019).

2.2.3. Numerical implementation

All numerical operations (generation and juniper of a mesh, building of matrix operators, Newton iteration for the base flow problem and the shift-invert method for eigenvalue problem) are handled thanks to the finite element software FREEFEM++ (Hecht 2012). The FEM discretization is built with the classical Taylor–Hood elements for all computations.

First, a triangular mesh is built using the well-known Delaunay–Voronoi algorithm, and a preliminary base flow and some modes are computed. An adaptive mesh strategy is adopted in order to ensure convergence of results with respect to mesh refinement, as it is described in Fabre *et al.* (2018). Namely, after first computing a base flow and an adjoint eigenmode, the mesh is adapted to both these fields, and the process is repeated twice. To demonstrate the efficiency of this method, we report in table 1 the eigenvalues computed with the adapted mesh and with an even more refined mesh obtained by adapting to both direct and adjoint modes and subsequently splitting all triangular cells in four. The results demonstrate that the mesh adaptation method provides converged results with a very reasonable mesh density and computational cost.

The whole computational chain, including mesh generation, adaptation, loop over parameters and post-processing, is monitored in the Matlab environment thanks to the STABFEM suite (Fabre *et al.* 2018), which is a set of MATLAB/OCTAVE drivers/wrappers specifically designed to perform such studies. A sample script reproducing a selection of results from the present study is available through the website of the STABFEM project (<https://stabfem.gitlab.io/StabFem>).

Mesh	λ	N_v	t_c [s]
Adapted	$1.1685 + 1.09952i$	6936	44
Split	$1.1686 + 1.09957i$	137374	2139

Table 1. Comparison of results found with a mesh build with the adaptation strategy and a refined one obtained by splitting. The table reports the number of the leading eigenvalue λ , the number of mesh vertices N_v and the computational time t_c (on a Macbook, 2Ghz, 32Go RAM, single processor) required for computing 10 modes with the shift-invert strategy, for the set of parameters $Re = 320$, $a/A = 0.75$, $L/d = 2$.

Section	L/d	a/A	Re	$ m $
III - A	2	0.01, 0.75, 0.81	320, 200–1200	1
III - B	2	0.01–0.92	320–1130, 110–400	1
III - C	2–10	0.01–0.75	110–140–200	1
III - D	2	0.6–0.92	80–1100	2–3

Table 2. Ranges of parameters investigated and corresponding sections of the paper.

2.3. Direct numerical simulations

To validate and to extend the results of the stability analysis, some full DNS are performed with the open source computational fluid dynamics software package, OpenFOAM®. Time-varying solutions of the (2.1) are computed with its incompressible finite volume solver, *pimpleFOAM*, built with a second-order spatial derivative scheme and an Euler temporal scheme. A fixed Courant number set to $Co = 0.5$ ensures the stability of these schemes. The meshes are built with the cfMesh software provided with OpenFOAM. A typical mesh and a mesh convergence study are presented in Appendix B. Results and comparison with LSA are discussed in § 4.

3. Linear stability analysis: results

With the objective of building an exhaustive cartography of instability properties, four parameters will be varied. The two first ones are geometrical parameters, namely the aspect ratio L/d and the confinement parameter a/A . The third input parameter is the Reynolds number and the fourth one is the azimuthal wavenumber m . Table 2 indicates the range of parameters defined for this study, and the concerned sections. Regarding the azimuthal wavenumber, it is known for open flows past blunt bodies that the most unstable modes are found for $m = \pm 1$ (Natarajan & Acrivos 1993; Auguste *et al.* 2010; Jiménez-González *et al.* 2014). This fact justifies that our study will primarily focus on this value. Other values of m are postponed to § 3.4.

3.1. $m = \pm 1$ modes for sample values of the section aspect ratio a/A

In this section and the next one we set the length-to-diameter aspect ratio $L/d = 2$ and we focus on the effect of the confinement ratio a/A .

3.1.1. Weakly confined flow

A weakly confined case is first considered, corresponding to section aspect ratio $a/A = 0.01$ (or diameter aspect ratio $d/D = 0.1$). Figure 2 displays the base flow around the

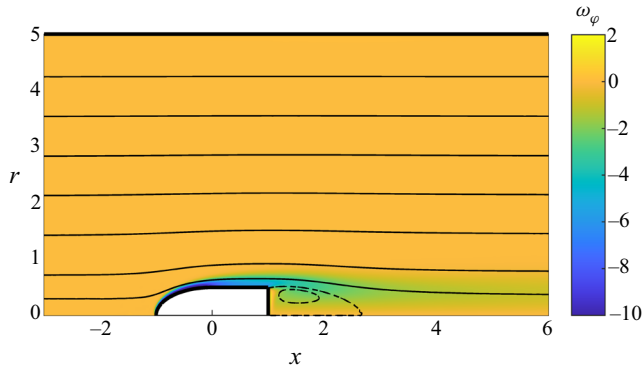


Figure 2. Azimuthal vorticity ($\omega_\varphi = \nabla \times \mathbf{u}_b \cdot \mathbf{e}_\varphi \equiv \partial_x u_r - \partial_r u_x$) and streamlines of the base flow for $Re = 320, L/d = 2, a/A = 0.01$.

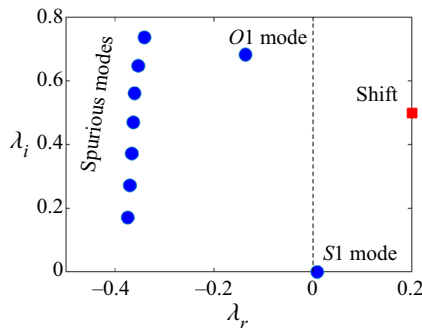


Figure 3. Example of a spectrum found with the shift and invert algorithm ($Re = 320, L/d = 2, a/A = 0.01$). The 10 eigenvalues closest to the ‘shift’ value indicated in red are computed.

blunt body for a Reynolds number $Re = 320$. The axisymmetric base flow field exhibits a standing eddy which has approximately the same length as the body itself. The boundary layer present on the body surface is made visible through the generation of negative azimuthal vorticity. Overall, this structure seems to be very similar to that found in Jiménez-González *et al.* (2014) for the same object and conditions in an unconfined flow.

For the same base flow, a part of the spectrum found using the LSA approach is shown in figure 3. It reveals two physical modes, the first one called *S1* is non-oscillating (often referred to as stationary) and unstable ($\lambda_r > 0$). The second one called *O1* is oscillating and damped. The other modes quasi-aligned are some spurious modes of a non-physical nature and come only from the numerical discretization. Similar results are observed by Jiménez-González *et al.* (2014) for a non-spinning object in unconfined space.

In their study, the onset of the first instability (the *S1* mode) was detected at a critical Reynolds number $Re_{c,S1} = 325.2$, whereas its value is $Re_{c,S1} = 312.2$ in the present study, leading to less than a four percent difference. It can be concluded that the confinement produces a small influence over the onset of the first instability in this case.

Figure 4 displays the four most amplified eigenvalues as a function of Re , again for $a/A = 0.01$. The first unstable mode appearing is non-oscillating and remains the most amplified mode over the whole range of Re studied. The second most amplified mode, *O1*, becomes unstable at $Re_{c,O1} = 478.3$ and $St_c = 0.103$. This Strouhal value is very close to

Flow past a bullet-shaped blunt body in a pipe

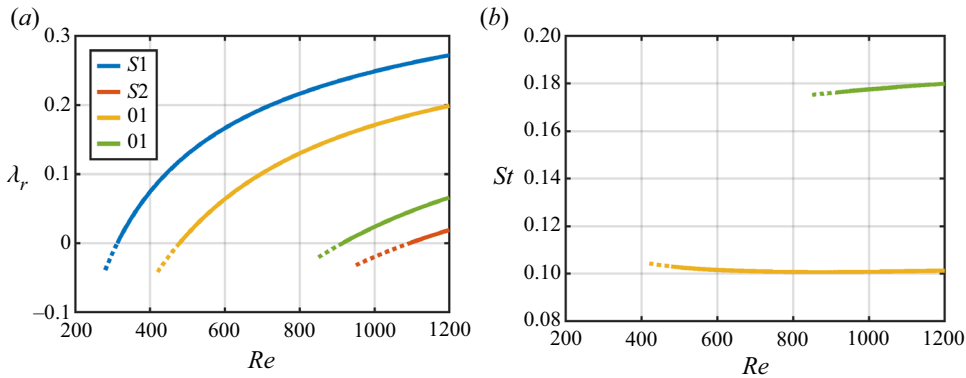


Figure 4. Amplification rate (a) and Strouhal number (b) as a function of the Reynolds number for the first unstable modes, $a/A = 0.01$, $L/d = 2$.

the one found by Bohorquez *et al.* (2011) who reported $St = 0.102$. But the latter authors found a somehow larger value of the critical Reynolds number, namely $Re_{c,O1} = 518$.

In addition to the effect of confinement, this gap between critical Reynolds number may be explained by the fact that the computational domain defined for the stability analysis included only the cylindrical rear of the body and excluded the nose in Bohorquez *et al.* (2011). The critical Reynolds is also notably higher than the one given by the reference case of a thin disk. The geometry of the nose of the blunt body changes the amount of vorticity produced at its surface, as pointed out by Brücker (2001), and it is known that this vorticity production is responsible for triggering the instabilities (Magnaudet & Mougin 2007). Having a profiled nose diminishes such production of vorticity and pushes back the onset of instabilities to larger Reynolds. For instance, in figure 2 the vorticity intensity for $Re = 320$ is $|\omega_\phi| \approx 10$, which is comparable to the intensity observed for a thin disk with aspect ratio $\chi = 3$ for $Re \approx 150$ as studied in Auguste *et al.* (2010).

Up to here, the main scenario revealed in the present configuration by the LSA is a first non-oscillating mode S1 amplification followed by an oscillating one O1. It is the same encountered for all axisymmetric bodies considered in the literature (Natarajan & Acrivos 1993; Meliga, Chomaz & Sipp 2009b; Tchoufag *et al.* 2014). When pushing the Reynolds number towards higher values, two additional modes are found, an oscillating one and a non-oscillating one termed O2 and S2. These higher modes arise at much larger Reynolds numbers, in the range $Re \in [900-1200]$. They are less likely to be observed experimentally or numerically because in such regimes the mean flow is already very far from the axisymmetric base flow analysed with the linear stability theory. Nevertheless, when the confinement effect is increased, these higher modes turn out to be relevant in order to obtain a consistent picture of the bifurcation scenario. Hence, they will be kept in the analysis and their critical Reynolds $Re_{c,S2}$ and $Re_{c,O2}$ will be tracked.

The structures of these modes are illustrated in figure 5. The plots display both the azimuthal velocity (colours) and pressure (lines) levels in a meridional (x, r)-plane (left plots) and the axial vorticity levels in a transverse (y, z)-plane corresponding to a cut at location $x = 2$ (right plots). The first unstable mode, S1, has a rather simple vorticity structure. In the meridional plane, the azimuthal vorticity of the eigenmode is positive in the region of the shear layer. Recalling that the vorticity of the base flow shear layer is negative (see figure 2), the effect of the eigenmode is to decrease in this region the net vortical intensity in the shear layer. Owing to the antisymmetry of

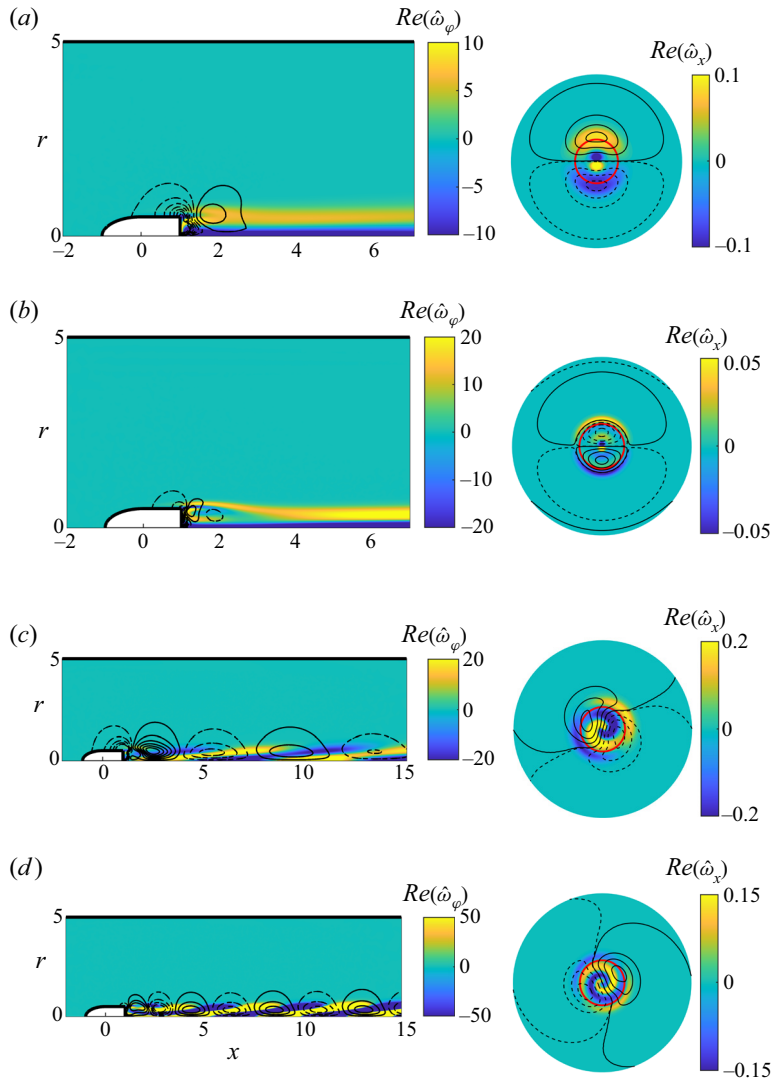


Figure 5. Eigenmodes found for $a/A = 0.01$, real parts of the vorticity with iso-levels of pressure. Slices are defined by $x = 2$ and $r \leq 2$. Results are shown for (a) $S1$, $Re = 320$; (b) $S2$, $Re = 1130$; (c) $O1$, $Re = 500$ and (d) $O2$, $Re = 950$.

$m = \pm 1$ modes, the azimuthal vorticity of the eigenmode is negative on the opposite side, meaning that the shear layer is enhanced. The axial vorticity, on the other hand, reveals a pair of counter-rotating streamwise vortices, as already noticed for disk and spheres (Natarajan & Acrivos 1993; Meliga *et al.* 2009b) and similar blunt bodies in open flow (Jiménez-González *et al.* 2014). The $S2$ mode shows a similar structure with a small additional pair of counter-rotating vortices in the vicinity of the blunt body rear, and a more complex pressure field than the $S1$ mode.

Let us now consider the oscillating modes $O1$ and $O2$ displayed in the bottom part of figure 5. One can observe in an azimuthal plane an alternation of positive and negative streamwise vorticity, which is the signature of unsteady vortex shedding. A shorter spatial wake length scale can be seen for the $O2$ mode, related to its higher shedding frequency

Flow past a bullet-shaped blunt body in a pipe

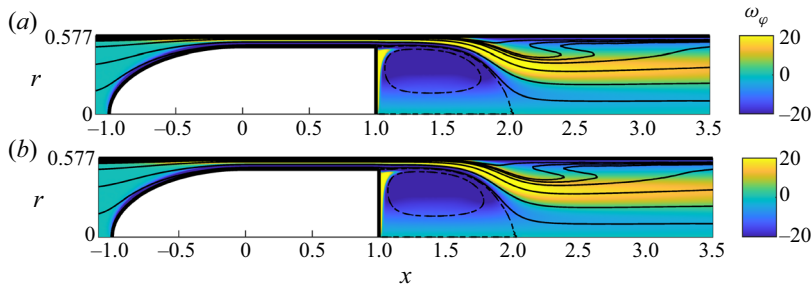


Figure 6. Azimuthal vorticity and streamlines of the base flow in the moving frame attached to the body for $L/d = 2$ and $a/A = 0.75$. Top, $Re = 110$, bottom $Re = 320$.

(i.e. larger St). Note that when observed in a transverse plane, these modes display a characteristic spiral structure. This does not imply that if these modes are present in a nonlinear solution a spiral structure will necessarily be observed. Indeed, it is known that due to the degeneracy associated to mirror symmetry, $m = +1$ and $m = -1$ eigenmodes are mirror images of each other and can lead to two kinds of nonlinear states (Fabre *et al.* 2008): (i) ‘rotating waves’ corresponding to a pure $m = +1$ (or $m = -1$) eigenmodes with a spiral structure, and (ii) ‘standing waves’ corresponding to superposition of $m = 1$ and $m = -1$ eigenmodes characterized by a symmetry plane.

3.1.2. Confined flow with $a/A = 0.75$

Let us now consider a more confined flow with a section ratio of $a/A = 0.75$ or a diameter ratio of $d/D = 0.87$. The structure of the base flow and the influence of the tube wall are displayed in figure 6. Compared with the unconfined or weakly confined flow, the recirculation length is shorter as the confinement becomes stronger. For Reynolds number $Re = 320$, the flow changes direction close to the pipe wall and goes downstream but without setting a closed recirculation zone attached to the wall, even for large values $Re > 320$. The presence of separation in this area is accompanied with a production of negative vorticity. This structure reveals the presence of a confined wall jet. Within the small gap between the body and pipe walls the flow can be seen as parallel and one may expect the flow to be well approximated by a parallel-flow solution called ‘annular Couette–Poiseuille flow.’ This classical solution is reproduced in Appendix A. The theoretical analytical non-dimensional velocity profile is compared in figure 7 to the actual axial flow profile extracted from the base flows represented in figure 6. At location $x = 0.75$ (in the rear part of the afterbody), the observed velocity profile is indistinguishable from the theoretical solution, both for Reynolds numbers $Re = 110$ and 320.

The velocity profile at location $x = 1.25$, slightly behind the body is also plotted in the figure. The curves show that the velocity profile turns into an annular jet, affected by some diffusion, especially for $Re = 110$.

The curves giving the amplification rate and the Strouhal number vs the Reynolds number as computed by the linear stability theory are displayed in figure 8, for the base flow solved with the section aspect ratio $a/A = 0.75$.

Three branches are found as the Reynolds number varies corresponding to two non-oscillating (called again $S1$ and $S2$) and one oscillating mode. The latter is of a distinct nature compared with the modes $O1$ and $O2$ previously encountered. It is characterized by a Strouhal number in a lower range, and it is thus called $O3$. The amplification curves of the $S1$ mode follows an inverted parabola: as the Re value increases, the amplification of the

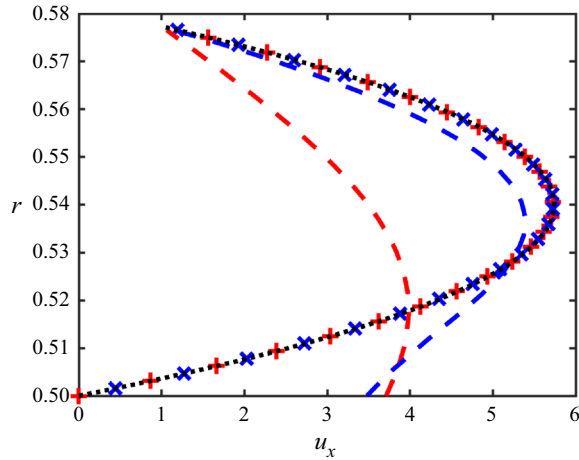


Figure 7. Axial velocity u_x as a function to r for $Re = 110$ (red) and $Re = 320$ (blue) at locations $x = 0.75$ (symbols) and $x = 1.25$ (dashed lines). Black dotted line: comparison with annular Poiseuille solution.

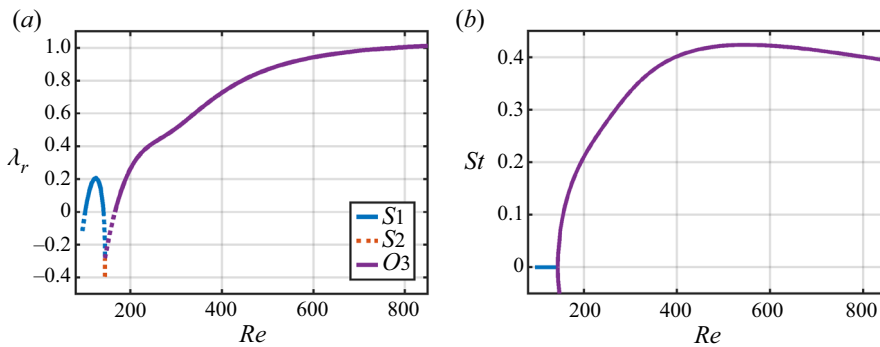


Figure 8. Amplification rate λ_r (a) and Strouhal number (b) vs the Reynolds number for the first unstable modes, $a/A = 0.75$. The horizontal range of the figure corresponds to $Re \in [80-1000]$.

$S1$ mode raises, reaches a maximum and decreases. The decreasing $S1$ branch meets the rising $S2$ branch and both branches collide at the Reynolds number $Re = 180.4$. Above this value, the collision gives rise to a pair of complex conjugate eigenvalues corresponding to the $O3$ oscillating mode. The symmetry of the problem entails that this oscillatory branch is twofold, for each eigenvalue λ found, $\bar{\lambda}$ is also an eigenvalue. The Strouhal number of the $O3$ raises strongly after the collision of $S1$ and $S2$ from $St = 0$ to $St = 0.1897$ at $Re = 490$ and then slightly decreases.

Figure 9 displays the vortical structure and some iso-pressure contours of the unstable eigenmodes for different values of the Reynolds number. The $S1$ and $S2$ modes exhibit the same behaviours found for the low confinement configuration, with a negative pressure zone at the rear of the blunt body followed by a positive pressure one.

Nevertheless, these pressure contours are distorted by the proximity of the pipe wall as the extrema get closer to the axis of symmetry. The vorticity of these two modes goes through the same changes and is more important close to the body.

The $S1$ mode is more active in the recirculation zone whereas for the $S2$ mode the azimuthal vorticity is higher in the region where the streamlines of the base flow expand,

Flow past a bullet-shaped blunt body in a pipe

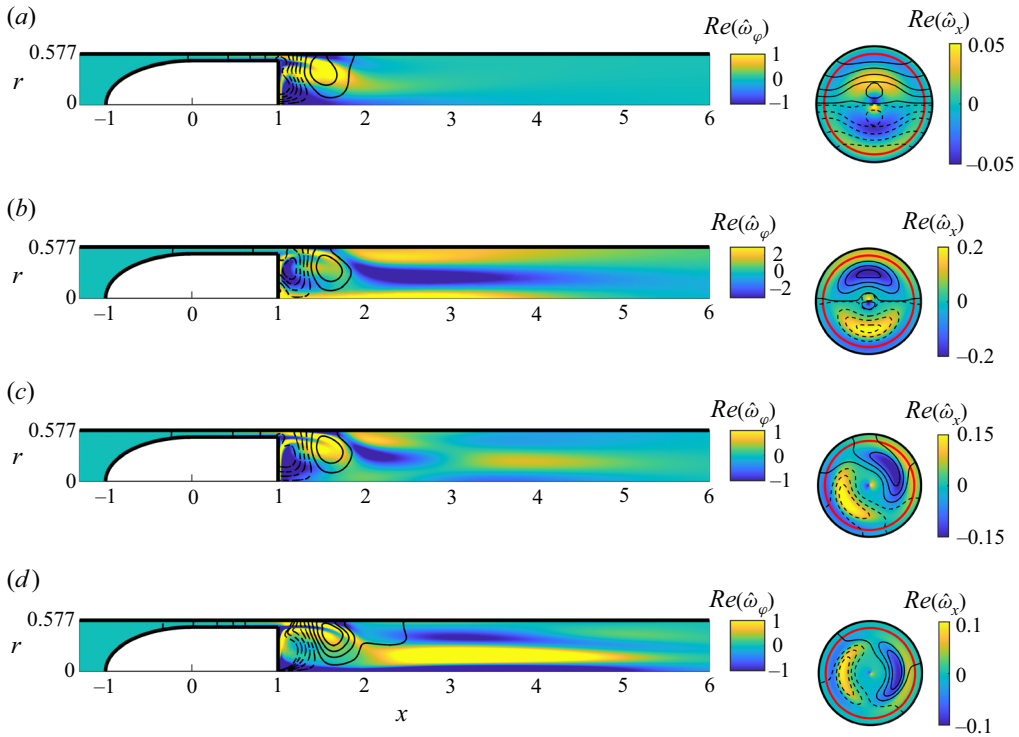


Figure 9. Eigenmodes found for $a/A = 0.75$, real parts of the streamwise vorticity with iso-levels of pressure. Results are shown for (a) $S1$, $Re = 110$; (b) $S2$, $Re = 117$; (c) $O3$, $Re = 200$ and (d) $O3$, $Re = 400$.

around $x = 2.5$, suggesting a different instability mechanism. At last, the structure of the $O3$ mode seems to be a mix of the $S1$ and $S2$ modes. The pattern of the vorticity and the pressure is very similar to the $S1$ mode in the recirculation zone. The downstream region ($x > 2$) is similar to the same region of the $S2$ mode but the temporal mode oscillation results in production of vorticity of alternated sign. For $Re = 400$, the influence of a larger recirculation zone can be noticed. Alternate values of vorticity in the streamwise direction are still present but they pushed downstream, outside the scope of the plot. Stronger vorticity is also observable because of an important contraction of the base flow due to its local reversal.

3.1.3. Strongly confined flow with $a/A = 0.81$

Consider now an even more strongly confined flow with a section ratio $a/A = 0.81$ or a length ratio $d/D = 0.9$.

The base flow (figure 10) remains very similar to the previous case but the bifurcation scenario revealed by the LSA approach seems different. Figure 11 displays the computed amplification rate and Strouhal number of the first three modes as a function of the Reynolds number. Again, two non-oscillating eigenmodes $S1$, $S2$ and an oscillating mode $O3$ are found. Here, the $S1$ mode becomes unstable between Reynolds numbers $Re_c = 101.1$ and $Re = 141.1$, the amplification rate plot keeps its inverted parabola shape. The $S2$ mode is observed as a stable mode up to $Re \approx 150$ where a collision with the $S1$ mode gives rise to a pair of complex eigenvalues corresponding to the $O3$ mode. The latter first arises as a stable mode, and subsequently becomes destabilized through a Hopf bifurcation

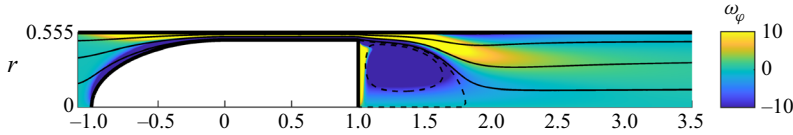


Figure 10. Azimuthal vorticity and streamlines of the base flow in the moving frame attached to the body for $L/d = 2$ and $a/A = 0.81$, $Re = 110$.

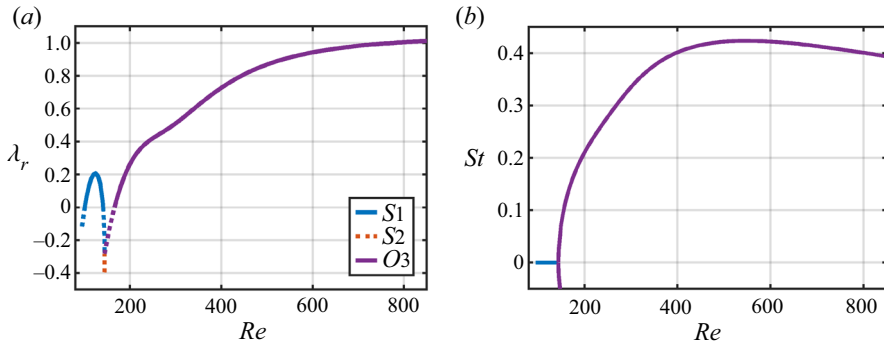


Figure 11. Amplification rate and Strouhal number for the three modes found for $L/d = 2$ and $a/A = 0.81$. The horizontal range of the figure corresponds to $Re \in [80–850]$.

at $Re = 166.2$. Then, $O3$ remains the predominant mode over the range of parameters studied. A stable pocket is present between the appearance of the $S1$ and $O3$ modes where the $S1$ and $S2$ branches collide, as they are both stable, forming the $O3$ branch. Note that the value of the dimensionless frequency of the $O3$ mode is twice the value of the previous case, $St = 0.4227$ at $Re = 550$. This fact is not really surprising since the maximum axial velocity in the jet (as predicted by the annular Couette–Poiseuille solution given in [Appendix A](#)) is about also twice the value of the previous case.

Considering the differences between the present case and the previous one, one can postulate the existence of an intermediate value of the confinement ratio where the collision of the $S1$ and $S2$ modes and the destabilization of the $O3$ mode will occur simultaneously. This situation, characterised by the existence of two simultaneous neutral modes with zero eigenvalues, corresponds to a codimension-two bifurcation of a Takens–Bogdanov type. This point will be confirmed in the parametric study of § 3.2.

To end up with characterisation of the $a/A = 0.81$ case, [figure 12](#) reveals the structure of the unstable modes $S1$ and $O3$. Observations made in the previous subsection for $a/A = 0.75$ apply here. We can add that the influence of the confinement is noticeable in the $S1$ mode as the maximum of velocity of the base flow is higher compared with the previous case. The $O3$ mode also possesses a patch of alternated sign of azimuthal vorticity exhibiting higher extrema than the previous case, for the same reason cited just above.

3.2. Cartography of $m = \pm 1$ modes in the $a/A–Re$ plane for $L/d = 2$.

A first exploration of the stability picture has been carried out for some selected values of a/A . The study is now extended continuously to a larger range of the confinement parameter with $a/A \in [0.01, 0.92]$. The azimuthal wavenumber of the perturbation and the length-to-diameter aspect ratio are kept respectively to $m = \mp 1$ and $L/d = 2$.

Flow past a bullet-shaped blunt body in a pipe

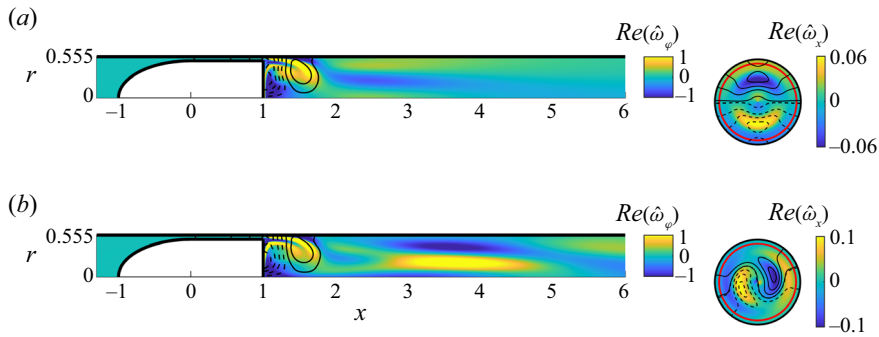


Figure 12. Eigenmodes found for $a/A = 0.81$, real parts of the vorticity with iso-levels of pressure. Slices are given for $x = 2$. Results are shown for (a) $S1$, $Re = 140$ and (b) $O3$, $Re = 200$.

The neutral stability curve for any mode is the location of zero amplification perturbations. For each value of the ratio a/A , a critical Strouhal number St_c and a critical Reynolds number are obtained which are the limit of the instability for any mode. The neutral curves are displayed in [figure 13](#) for the six modes of interest. The map is built by following the branches in the parameter space with a step in confinement ratio of $\Delta(a/A) = 0.001$ and/or a Reynolds number increment of $\Delta Re = 1$. A strategy has been developed to ensure continuous and accurate values of the curve. A first sweep of the $(Re, a/A)$ plane is initially performed to save computational time. Then thorough computations are conducted following unstable branches. For each confinement value, Re is increased in order to find lower and upper bounds of its critical value Re_c , and a linear interpolation is completed to get a more accurate value such as $\lambda_r(Re_c) = 0$.

The first important result observed from this figure is about the destabilization of the axisymmetric base flow. It is always caused by the same $S1$ mode for all area ratios a/A in the range 0.01 to 0.92. The loss of axial symmetry always occurs through a stationary bifurcation.

The deep stability analysis has also revealed the existence, for the secondary modes, of two different regimes and a transition zone. First, in the weakly confined regime, up to $a/A < 0.7$, the secondary dominant mode is the $O1$ mode, and higher modes ($S2$, $O2$) arise in a much larger range of Reynolds number which makes their physical relevance unlikely. In addition, the sequence of instabilities with a non-oscillating $S1$ mode followed by an oscillating $O1$ mode is thus the same as observed for other blunt bodies in free-stream flow (Natarajan & Acrivos 1993; Fabre *et al.* 2008; Meliga *et al.* 2009b; Auguste *et al.* 2010). The confinement is also found to be destabilizing for both these modes, as the critical Reynolds thresholds decrease as the confinement ratio a/A grows. Large confinement also increases the frequency of the oscillating $O1$ mode, consistent with the fact that the mean velocity of the annular jet formed past the body increases with the confinement (for a given flow rate, a decreasing section increases velocity).

A transition regime is observed in the interval $0.7 < a/A < 0.76$. The threshold of the $S2$ mode first decreases after $a/A \approx 0.6$ to approach that of the $O1$ mode. The latter is then strongly and abruptly stabilized, and it is no longer found for $a/A > 0.72$. In the range $0.72 < a/A < 0.76$ the stationary $S2$ mode becomes the dominant secondary mode.

The strongly confined regime occurs for a/A greater than 0.76. At this regime, the oscillating modes $O1$ and $O2$ are no longer present and new ones ($O3$, $O4$) appear with low or moderate dimensionless frequency. Let us follow in [figure 13](#) the mode evolution along a vertical line at a/A close to 0.86 and consider the evolution when increasing the

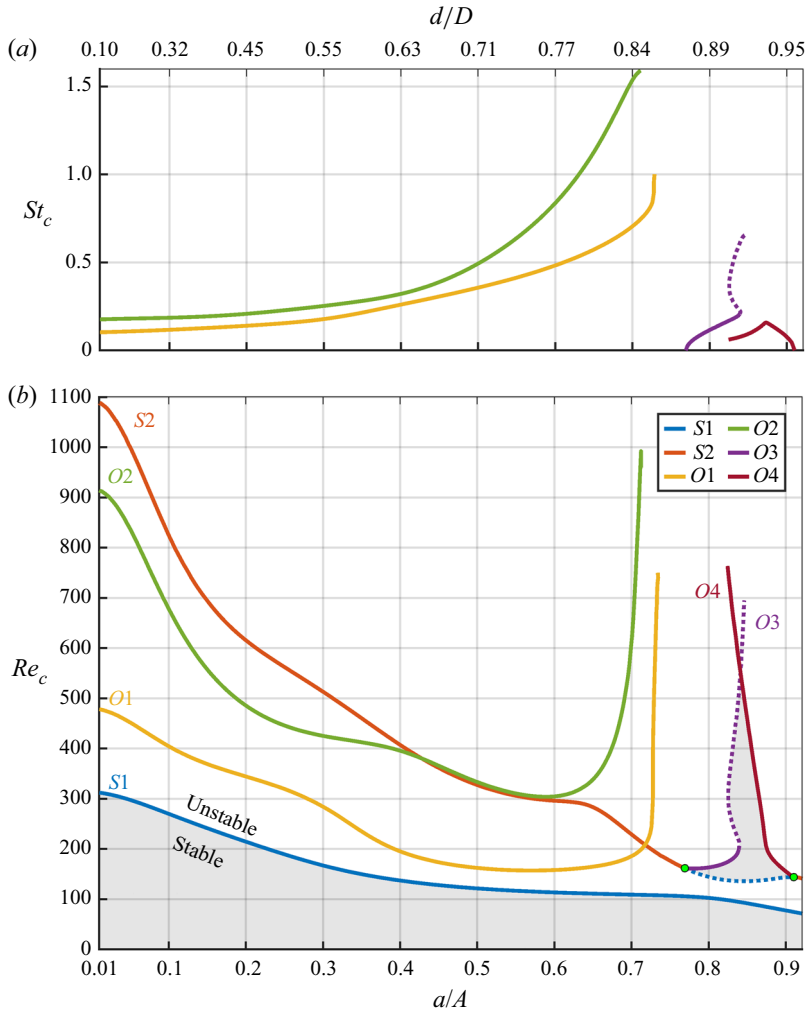


Figure 13. Neutral curves in the $Re - a/A$ plane, and critical Strouhal number as a function of the confinement ratio. The body length is kept constant, $L/d = 2$. The dashed portions of the blue and purple curves are part of the neutral curves corresponding to restabilization of the S1 and O3 modes.

Reynolds number. It can be seen that the initially stable S1 mode becomes unstable on a short range of Re , then it is unstable in a larger range of Re , and finally the flow instability is generated by the appearance of the modes O3 and O4. In a short area, coloured in grey in the figure, a pocket of stability is found. It can be noticed that the neutral curve of the O3 mode also displays two turning points close to $Re_c \approx 200$. So in a narrow range around $a/A = 0.84$, the destabilization/restabilization sequence occurs twice as Re is raised. The complexity of the stability diagram for very strong confinement is a translation of the real physics complexity in this region with a fast annular wall jet, separated flows and vortical interactions.

As already discussed, the emergence of the stable pocket is expected to be associated to a codimension-two bifurcation of Takens–Bogdanov type, where both S1 and S2 modes are simultaneously neutral. This statement is confirmed in figure 13, as indicated by the green point with coordinates $(a/A, Re_c)_{TB}^{O3} = (0.769, 161.57)$ from which the O3 neutral

curve emerges. Note that a second Takens–Bogdanov point is observed at coordinates $(a/A, Re_c)_{TB}^{O4} = (0.91, 143.96)$. The latter bounds the stable pocket on the other side and is associated to the emergence of the $O4$ mode. As indicated in the upper plot, the critical Strouhal number of $O3$ and $O4$ modes is zero at the codimension-two points, as expected for a Takens–Bogdanov bifurcation. The Strouhal numbers of these modes raise as one moves away from these points.

3.3. Effect of the L/d aspect ratio

The effect of the length-to-diameter ratio L/d of the blunt body is now investigated keeping again the restriction to $m = \pm 1$ modes. This geometrical parameter is found to modify the stability properties only in the weakly confined regime at $a/A < 0.7$ identified above. Consequently, only the neutral curves of the modes $S1$, $S2$, $O1$ and $O2$ relevant to this regime are tracked. The neutral curves of these modes are shown in [figure 14](#) for different values of $L/d = \{4, 6, 8, 10\}$. They are compared with the results of the reference case with $L/d = 2$ presented in the previous paragraph (in green in [figure 14](#)). For low confinement, $a/A < 0.4$, the increase of the body length stabilizes the flow as pointed out by Brücker (2001) in his experiments. He suggests a larger boundary thickness caused by a longer body is responsible for this stabilizing effect. To verify this argument, [figure 15](#) (left plot) shows the vorticity at the blunt body surface for different body lengths. On the ellipsoidal nose ($x < 0$), the plots are superposed indicating the generation of the same amount of vorticity. Then, on the cylindrical surface of the blunt body ($x > 0$), the vorticity reaches a higher value for short objects. Indeed, a streamline along the body and its recirculation zone is more curved for short objects, accumulating therefore more vorticity feeding the separated flow in the rear.

In conclusion, for shorter objects, the recirculation zone generates stronger reverse velocities (see [figure 15](#), right plot), promoting wake instabilities at lower Reynolds number compared with the case of longer objects. We can also note that even if the vorticity intensities are quite different, their sizes do not differ so much.

Back to [figure 14](#), as the area ratio increases, all curves tend to collapse into one, either the Re_c or the St_c . It means that, for $a/A > 0.4$, the body length does not have influence on the onset of the four investigated instability modes. This is consistent with the fact that, as verified in [figure 7](#), once a certain confinement is reached and whatever the length of the body, the velocity profile is the same and corresponds to the annular Couette–Poiseuille solution recalled in [Appendix A](#).

3.4. Higher azimuthal wavenumber modes

To complete the parametric study, we now consider eigenmodes with azimuthal wavenumbers other than ± 1 . No axisymmetric ($m = 0$) unstable mode is found, but numerous unstable modes with $|m| > 1$ are detected. Most of them occur in ranges of Reynolds number far above the primary threshold of $m = \pm 1$ modes so they are not likely to be observed in any real flow. Only two modes were detected with a critical Reynolds number in the same range as $m = \pm 1$ modes. Both of them are non-oscillating, with respectively $m = 2, 3$ azimuthal wavenumbers, and will be referred to as $S_{m=2}$ and $S_{m=3}$. These modes arise in the strongly confined regime $a/A > 0.6$ where the length of the body has a negligible effect. In this section we keep the body aspect ratio $L/d = 2$ but conclusions given in this paragraph actually hold for all values of L/d .

The structure of these new eigenmodes are illustrated in [figure 16](#). Their geometry is best understood by looking at the views in a transverse x -plane (plots in the right column).

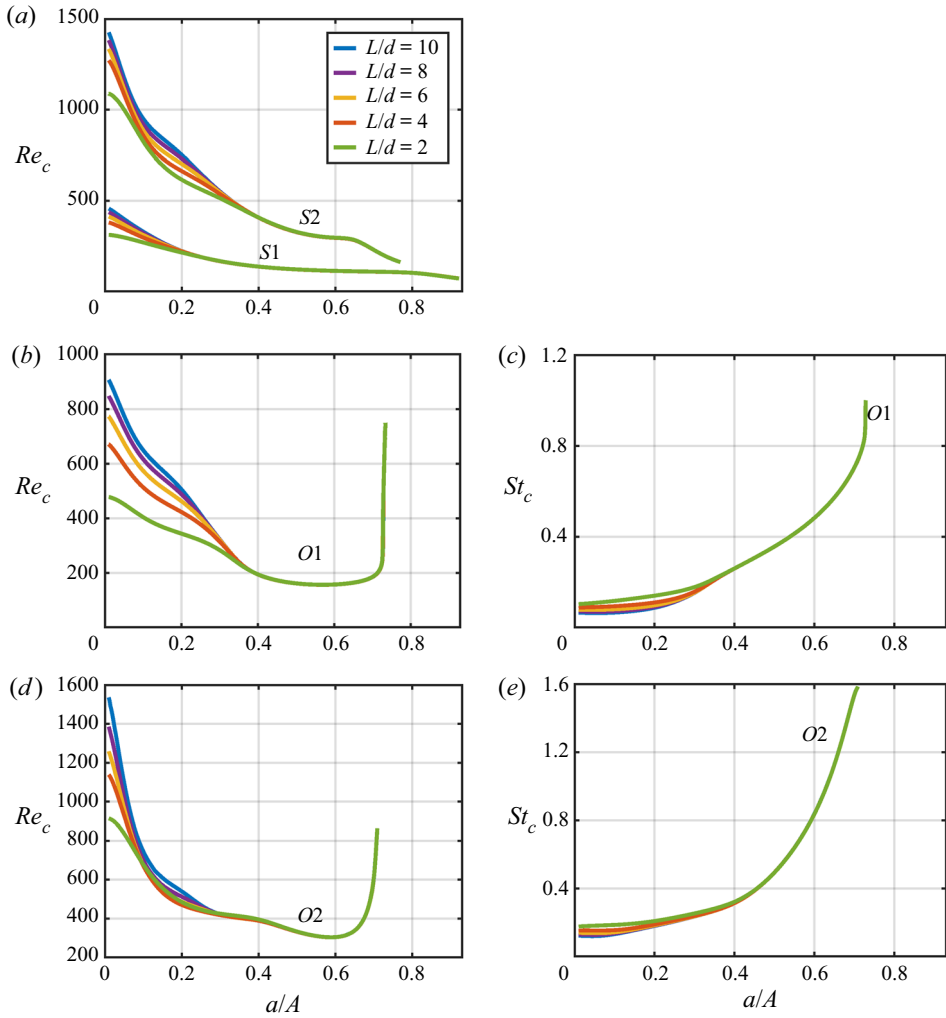


Figure 14. Neutral curves of the stationary modes for different body lengths.

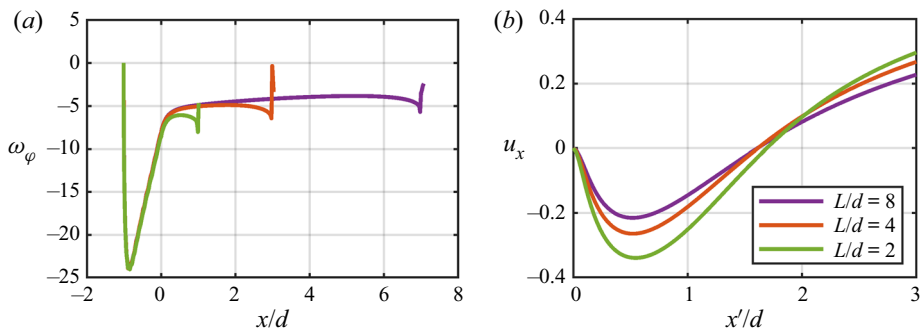


Figure 15. Left, azimuthal vorticity of the base flow at the blunt body surface for $Re = 330$. Right, axial velocity downstream the blunt body, the frame has been shifted in order to set the rear of the bodies at the same location. Only the base flow for $L/d = 2$ has an unstable mode S1.

Flow past a bullet-shaped blunt body in a pipe

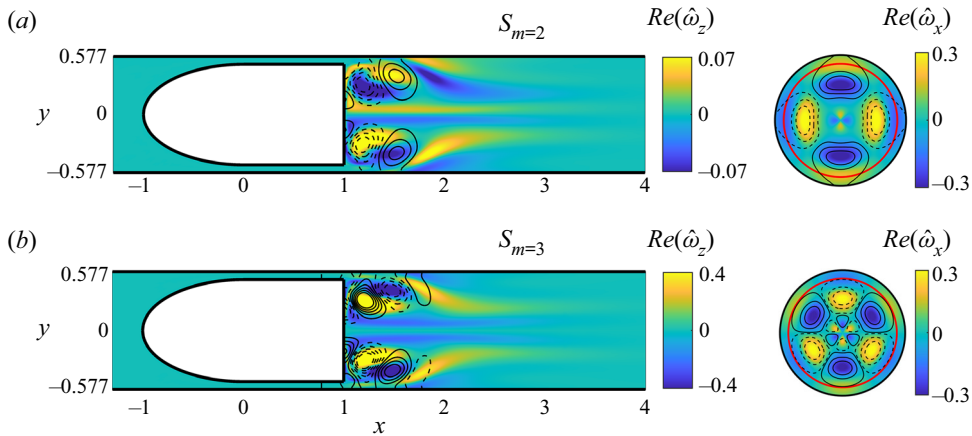


Figure 16. Unstable non-oscillating modes at $Re = 200$ and $a/A = 0.75$. Left: z -component of the vorticity and iso-level of pressure. Right: slice in the transverse plane at $x = 2$, streamwise component of the vorticity and iso-levels of pressure, the red circle represents the projection of the base of the blunt body in this plane.

Mode $O2$ is characterised by the existence of two orthogonal symmetry planes and displays four main structures of axial vorticity of alternated signs, while mode $O3$ has three planes of symmetry and six main vorticity structures. Secondary vorticity structures of opposed signs are also visible near the symmetry axis. The views in a vertical plane (left column) give a complementary picture. One can notice that compared with $m = \pm 1$ eigenmodes the present ones are more localized in the close wake and do not extend in the far wake.

The neutral curves in the $(Re_c, a/A)$ plane of the modes computed for $m = \{1, 2, 3\}$ are plotted in figure 17 which completes the results of figure 13 with additional azimuthal wavenumbers. The Strouhal numbers are not displayed because the newly considered modes are stationary, $St_c = 0$. For a low confinement, the stationary modes $S_{m=2}$ and $S_{m=3}$ have critical Reynolds numbers much higher than the first unstable mode and they are rather unlikely to be observed in real experiments. However, as the confinement increases, their critical Reynolds number Re_c decreases, and they alternatively become the second and third mode to be unstable for $a/A > 0.7$. Interestingly, in this strongly confined regime, these two modes become unstable for Reynolds number values very close to those corresponding to restabilization of the $S1$ mode. Hence, in such ranges they are the only unstable modes to exist. So non-axisymmetric flow characterised by azimuthal wavenumber $m = 2$ or 3 (or a superposition of both) are expected to be observed without the presence of any $m = 1$ component in experiments or simulations. Such structures are characterised by the absence of lift forces exerted on the body, as justified, for instance, in Tchoufag *et al.* (2014). Only $m = \pm 1$ modes can contribute to a lift force.

4. Exploration of nonlinear dynamics using DNS

In the previous section an exhaustive mapping of the linear stability characteristics of the flow with respect to the aspect ratios and the Reynolds number has been performed. In this section the nonlinear dynamics is now explored using DNS. The aim is both to confirm the LSA predictions regarding the primary instability threshold and to investigate the nonlinear dynamics arising away from this threshold.

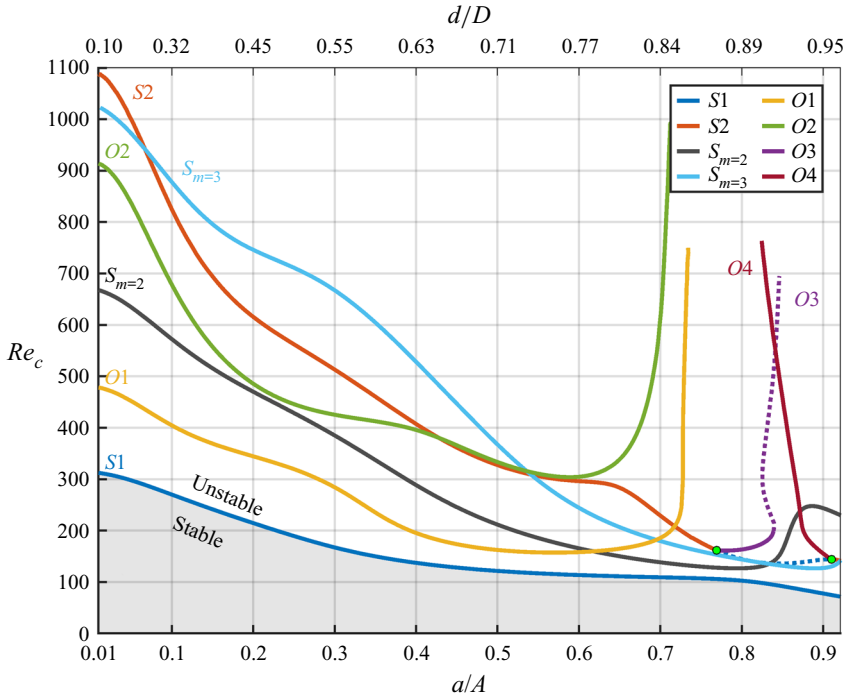


Figure 17. Critical Reynolds number as a function of the confinement ratio for all modes considered. The body length is kept constant, $L/d = 2$.

4.1. Dynamical regimes detected by DNS and comparison with LSA

In the numerical exploration we selected five values of the confinement ratio a/A covering the different regimes indicated by LSA, and ranges of Re from slightly below the primary threshold found by LSA to about twice this value. The conducted simulation runs are given by their coordinates in the parametric plane ($Re - a/A$) in figure 18.

Five general kinds of solutions are observed and are displayed using different symbols. The first kind (white squares) is an axially symmetric state corresponding to a stable configuration with zero lift \mathcal{L} , i.e. the lift coefficient $C_\ell = \mathcal{L}/1/2\rho U_\infty \pi r^2$ is measured lower than 10^{-4} . The second (black squares) is a three-dimensional steady state characterised by a constant lift and a symmetry plane. This state is noted SS_1 as its structure is a strong indication of the direct effect of a steady $|m = \pm 1$ eigenmode. The third (black circles) is a RSP state. This mode is defined by an oscillatory lift around a non-zero mean value, the wake still displaying a planar symmetry. Aperiodic behaviours (black stars) have also been observed. Finally, the fourth kind of solutions (black triangle, noted SS_3) are steady states with a structure characterised by an $m = 3$ component.

The LSA predictions are reproduced in figure 18 to allow a comparison with DNS results. The transition from the axisymmetric state and the steady non-axisymmetric state SS_1 revealed by DNS is observed to be well predicted by the marginal stability curve $Re_{c,S1}(a/A)$, indicating destabilization of the S_1 modes. This fully confirms that the nonlinear state SS_1 is effectively directly due to a supercritical nonlinear saturation of the S_1 mode.

On the other hand, in the computed cases, the observed secondary bifurcations (leading either to a periodic RSP state or to an aperiodic state), does not directly match with

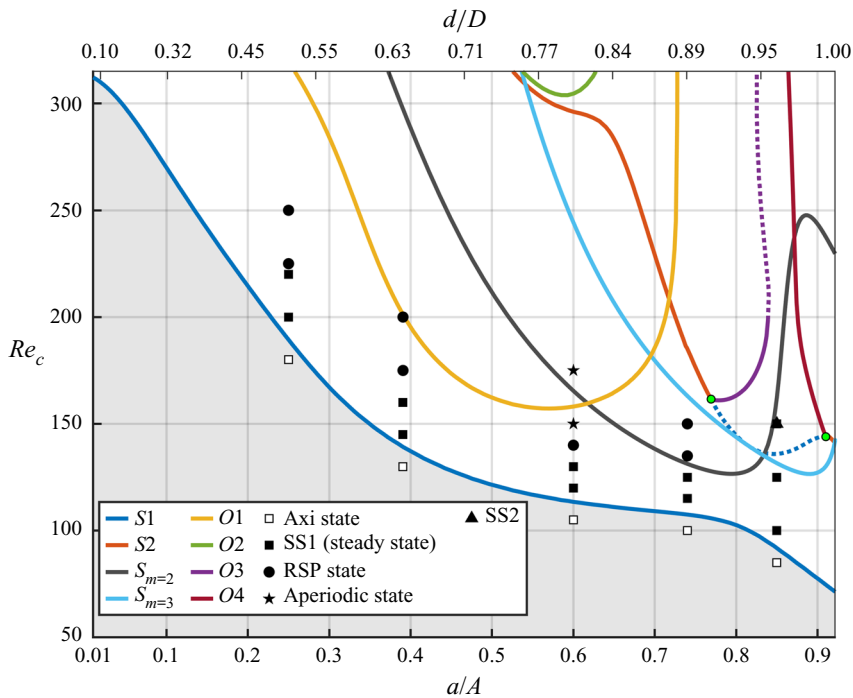


Figure 18. Neutral curves computed previously using LSA and DNS results represented by the symbols.

any secondary bifurcation curve found by LSA. This is not really surprising, since the secondary bifurcation occurs along the bifurcated steady state mode (SS) which differs from the axisymmetric solution used as a base flow for the LSA. However, the nature of the secondary modes revealed by LSA may still be relevant to fully explain the nonlinear dynamics, as it will be demonstrated by a deeper exploration of few cases in the next section.

4.2. Towards nonlinear behaviour, low confinement flow at $a/A = 0.39$

The temporal evolution of the wake for different Reynolds number and for a fixed area ratio are now analysed with DNS. Figure 19 displays the Q-criterion for the four Reynolds numbers $Re = 130, 145, 175, 200$, with two plots for each case corresponding to the view in two orthogonal directions.

For $Re = 130$ (figure 19a), the flow corresponds to the axially symmetric state, in accordance with the LSA prediction. The wake is axially symmetric and the view is identical in both orthogonal directions. The structure behind the blunt body is stationary and it consists of a toroidal recirculation bubble. For $Re = 160$ (figure 19b), the SS1 steady, non-axisymmetric state is observed. The loss of axisymmetry results in a tilting of the toroidal structure attached to the body, the latter expanding in one direction and retracting in the opposite one.

The next states for $Re = 175$ and $Re = 200$ (figure 19c,d) correspond to the RSP oscillatory state. The toroidal recirculation gets destabilized and hairpin vortices are periodically advected in the streamwise direction. The interaction between those vortices and the wall is visible through wall shaped vortices which merge with the hairpin vortices as they move downstream.

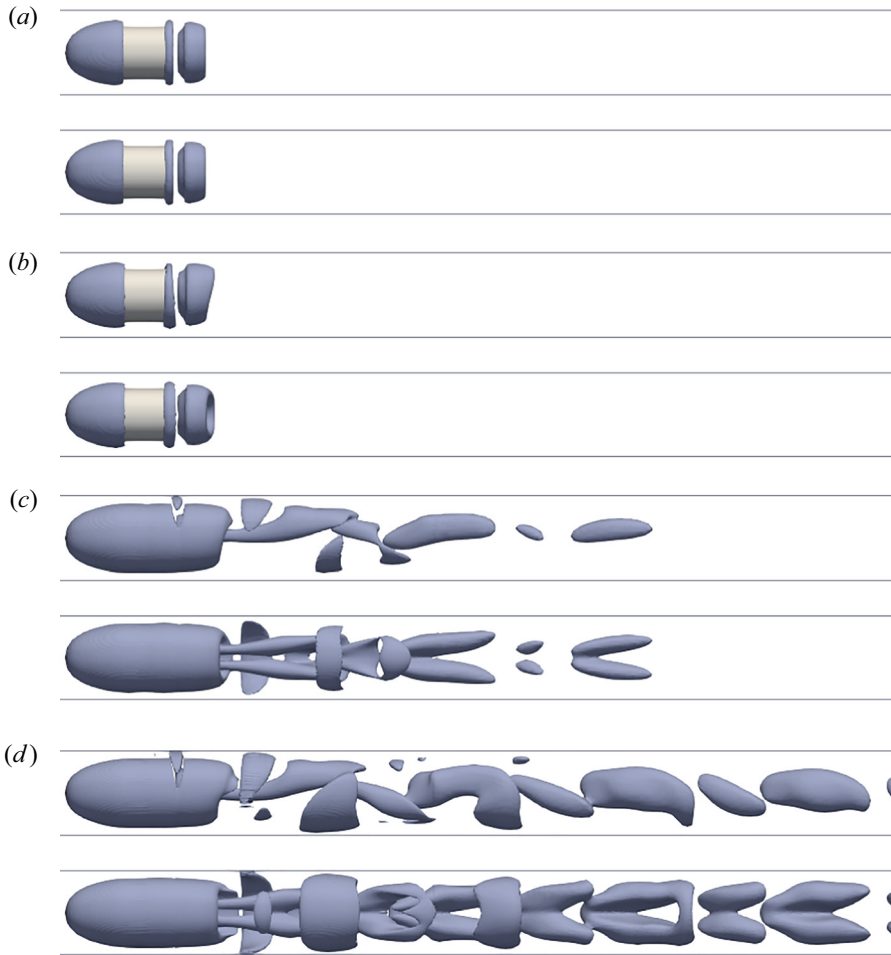


Figure 19. Iso-contour of Q-criterion for $a/A = 0.39$, two perpendicular views are represented for each case. From top to bottom, $Re = 130, 145, 175, 200$.

Up to here, the sequence of bifurcations and the structure of the observed states are identical to the unconfined case (Bohorquez *et al.* 2011; Bury & Jardin 2012). The main difference is that due to confinement, the bifurcations arise at a much lower Reynolds number value. For instance, Bohorquez *et al.* (2011) report the first bifurcation for $Re = 319$ and the second for $Re = 413$.

Figure 20 displays the time history of the lift and drag coefficients (noted C_ℓ and C_d) characterising forces exerted on the body calculated from DNS, again for $a/A = 0.39$.

For $Re = 130$ (case not displayed), the lift converges to a zero value. For all other cases, after a short transient (not shown), the simulations first seem to converge towards a steady state with zero lift, approximately in the range $t \in [30-50]$. The later evolution shows however that this state is not stable, and a phase of linear instability characterised by exponential growth of both coefficients is seen. In this linear phase the observed behaviour of the lift coefficient corresponds to a purely exponential growth with non-oscillating behaviour ($\approx e^{\sigma t}$ with real σ). This is a clear signature of the emergence of the non-oscillating mode S1 which is effectively the only unstable one detected by LSA for the values of considered Re .

Flow past a bullet-shaped blunt body in a pipe

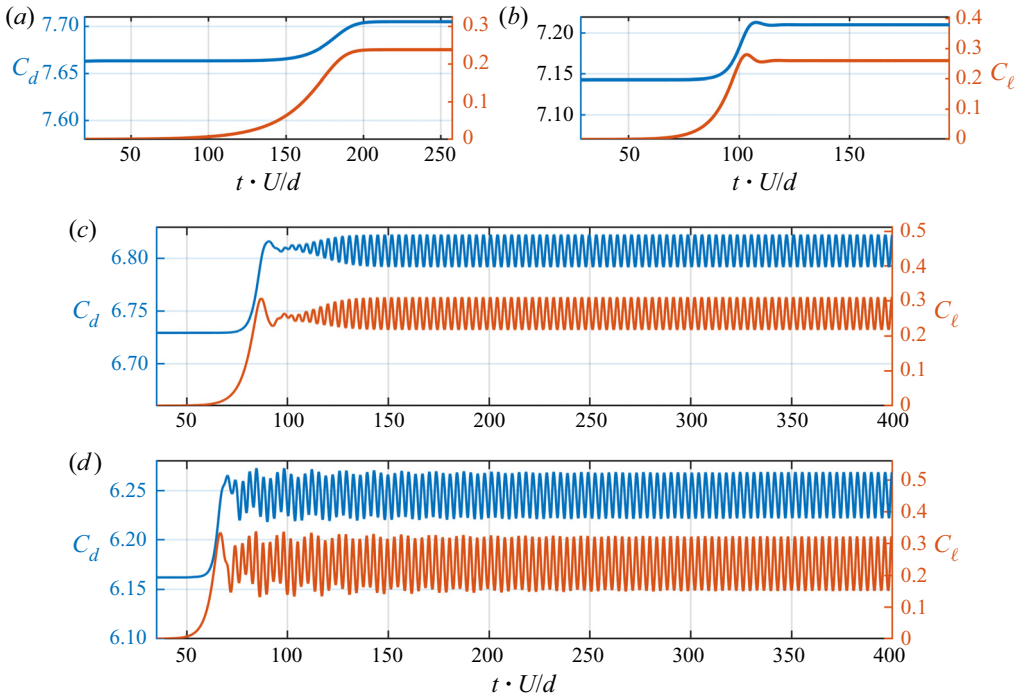


Figure 20. Lift and drag coefficients from DNS simulations ($L/d = 2$ and $a/A = 0.39$) vs dimensionless time, for (a) $Re = 145$, (b) $Re = 160$, (c) $Re = 175$ and (d) $Re = 200$.

For $Re = 145$ (figure 20a) and for $Re = 160$ (figure 20b), the subsequent nonlinear evolution is a saturation towards the SS1 steady state with non-zero lift. On the other hand, for $Re = 175$ (figure 20c), this steady state seems to be transiently approached by the solution, but then a second phase of linear instability follows, this time with oscillating behaviour ($\approx e^{\sigma t}$ with complex σ) is observed. This trend is the signature of the existence of a non-oscillating mode related to the $O1$ mode. For $Re = 175$, the saturated state ultimately observed is the periodic, RSP state characterised by a lift force oscillating around a non-zero mean value. For $Re = 200$ (figure 20d), the initial behaviour and ultimate state are similar, but transient towards the RSP state and displays a low-frequency modulation which is eventually damped.

The dimensionless frequency spectra of the two oscillating cases are presented in figure 21. They are performed from the C_ℓ signal of figure 20 and the transitional behaviours have been excluded. It has been verified that the sample is large enough and does not influence the spectra. Both spectra lead to similar observations. The two peaks can be interpreted as a fundamental frequency mode and its first harmonic. The amplitude of the first harmonic is much lower than the fundamental and, therefore, it is not visible to the naked eye on the signal which is very close to a pure sinusoid. As shown in the table found in figure 21(c), the influence of the Reynolds number on the Strouhal number St is weak with this Re range, DNS give a 2% variation between $Re = 175$ and 200. This behaviour is substantiated by the quasi-constant St values found using the LSA for low confinement (see figure 4b). The St values given by DNS and LSA approaches are comparable even if a 16% relative difference is measured between DNS ($Re = 200$) and LSA at the threshold ($Re = 201.2$). The discrepancy between these results can be explained by the fact that the $O1$ mode is obtained using an axially symmetric base flow whereas this base flow is no

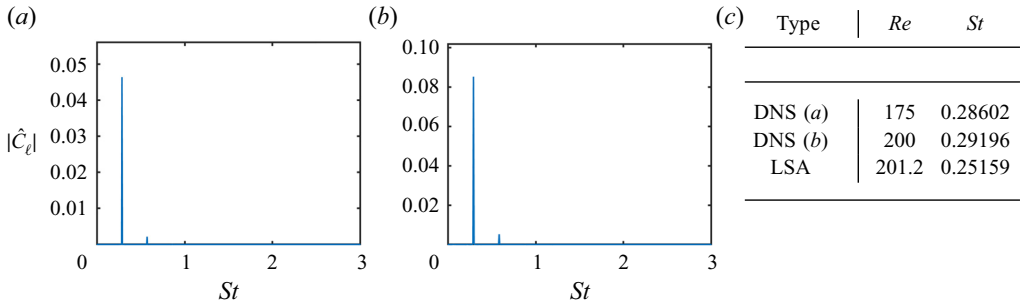


Figure 21. Frequency spectra for DNS case $L/d = 2$, $a/A = 0.39$, $Re = 175$ (a), $Re = 200$ (b) and table of St values of the higher peaks (DNS) with corresponding St_c for LSA (c).

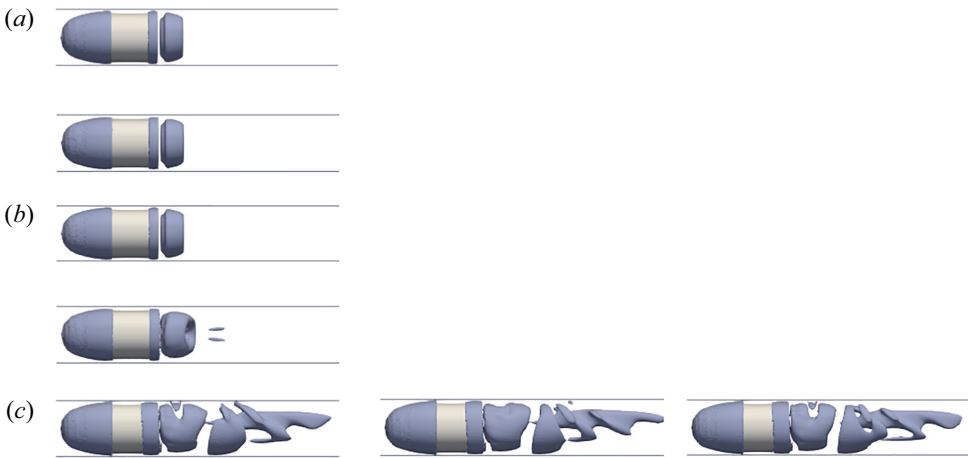


Figure 22. Iso-contour of Q-criterion for moderately confined cases; two perpendicular views are represented for each case: (a) $a/A = 0.74$, $Re = 100$; (b) $a/A = 0.74$, $Re = 115$; (c) $a/A = 0.74$, $Re = 160$. For the last case, instantaneous representations for three different instants are displayed.

longer present in the DNS for $Re \geq 175$, the RSP state oscillates around steady state which is non-axisymmetric.

4.3. Towards nonlinear behaviours, moderately confined cases ($a/A = 0.6$ and 0.74)

Consider, now, the flow structures revealed by DNS in the range of moderately confined cases. The beginning of the bifurcation sequence is the same as described in the previous paragraph. With an initially symmetric state, followed by a steady, non-axisymmetric state. Figure 22(a,b) displays these two states observed respectively for $a/A = 0.74$; $Re = 100$ and $a/A = 0.74$; $Re = 115$. Similar structures are obtained for $a/A = 0.6$ and the same values of Re and are not displayed.

When raising the Reynolds number to $Re = 150$ in this range of moderately confined cases, nonlinearities lead to richer dynamics compared with the previous cases. Consider, first, the flow obtained for $a/A = 0.74$ (figure 22c). Although the flow symmetries still indicate the (RSP) oscillatory state, the flow has a more complex structure than previously observed. Two main oscillating regions can be seen: the first one is the upper part of toroidal recirculation, close to the body, where a separated structure periodically appears. The second one is formed by a more distant structure, a 45° -inclined protrusion which is

Flow past a bullet-shaped blunt body in a pipe

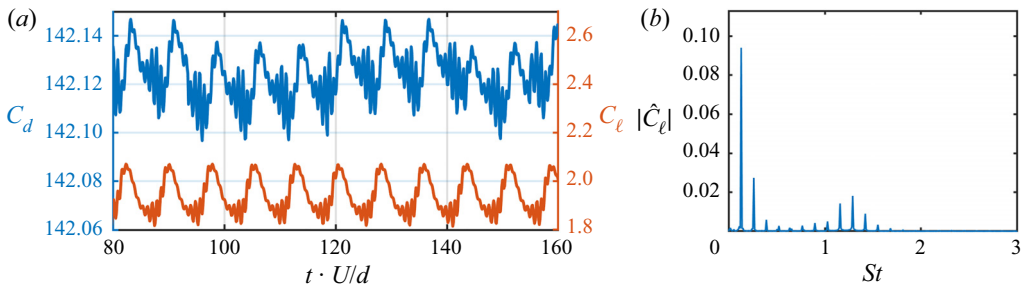


Figure 23. Characterisation of time-dependent forces exerted on the body for $Re = 150$, $a/A = 0.74$: (a) time history of lift and drag coefficients, and (b) frequency spectrum of the lift coefficient.

advected downstream. Sticking to the case $a/A = 0.74$, $Re = 150$, figure 23(a) displays the time history of the lift and drag coefficients. The lift force shows a temporal modulation where both a low-frequency component (with dimensionless period of order 7.5) and a high-frequency component (with a period about 10 times shorter) can be discerned. The drag coefficient displays similar patterns but the amplitude of oscillations are extremely small (less than 0, 5 % of the average value).

Although the time series may suggest a quasi-periodic behaviour, analysis of the Fourier transform of the lift force (figure 23b) indicates that the behaviour is actually strictly periodic, as demonstrated by the existence of a fundamental frequency, $St_1 = 0.1308$ along with its harmonics. The spectrum also shows that apart from the fundamental, a high-frequency content is centred around the harmonic number 10, corresponding to $St_{10} = 1.308$. This matches with the high-frequency component detected in the time series with a period about 10 times shorter compared with the low-frequency component.

Trying to relate these dynamics to the LSA results is a bit puzzling; going back to figure 13 shows that no unsteady modes exist for $a/A = 0.74$ since $O1$ and $O2$ are only detected for $a/A < 0.73$ and the low-frequency $O3$ mode only arises for $a/A > 0.75$. However, again, the results obtained from LSA considering the axisymmetric base flow are only indicative here since the bifurcations arise from the steady non-axisymmetric state. The order of magnitude of the Strouhal number St_1 characterising the low-frequency oscillation is in the same range as the $O3$ mode which exists for $St \approx 0.1-0.2$, suggesting that the $O3$ mode actually plays a role in the nonlinear solution given by DNS.

Consider, now, the flow obtained for $a/A = 0.6$ and $Re = 150$. The time series of the exerted forces (figure 24a) show that periodicity is clearly lost and indicate a chaotic behaviour. This is confirmed by examining the Fourier transform of the lift force (figure 24b) which now shows a broadband spectrum.

4.4. Towards nonlinear behaviours, high confinement flow at $a/A = 0.85$

To end up the exploration of nonlinear dynamics, consider now a highly confined case with $a/A = 0.81$. The first bifurcation again leads to the steady, non-axisymmetric state and is well explained by the onset of mode $S1$. On the other hand, when raising the Reynolds number, the next bifurcation does not lead to time-dependent vortex shedding. Instead, the flow remains stationary, but it acquires a structure characterised by the shedding of six vortical structures compared with only two as in the $SS1$ state, as shown in figure 25(a) for $Re = 150$. This structure is a strong indication of the presence of an eigenmode with azimuthal wavenumber $m = 3$, and it is in accordance with the LSA results which indeed predict the existence of the steady mode $S3$ in the same range of parameters. Plotting

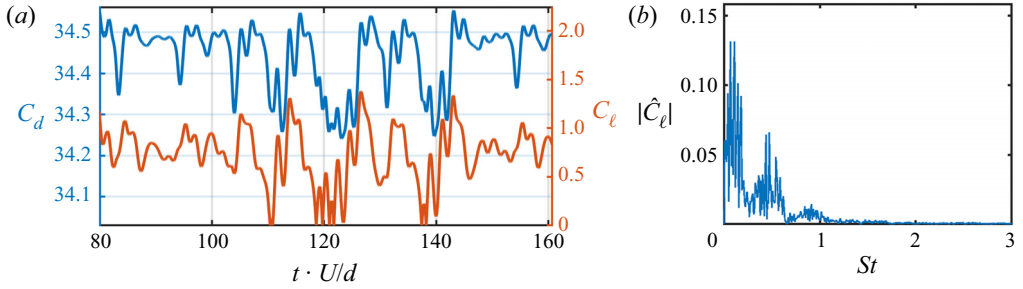


Figure 24. Characterisation of time-dependent forces exerted on the body for $Re = 150$, $a/A = 0.6$: (a) time history of lift and drag coefficients, and (b) frequency spectrum of lift coefficient.

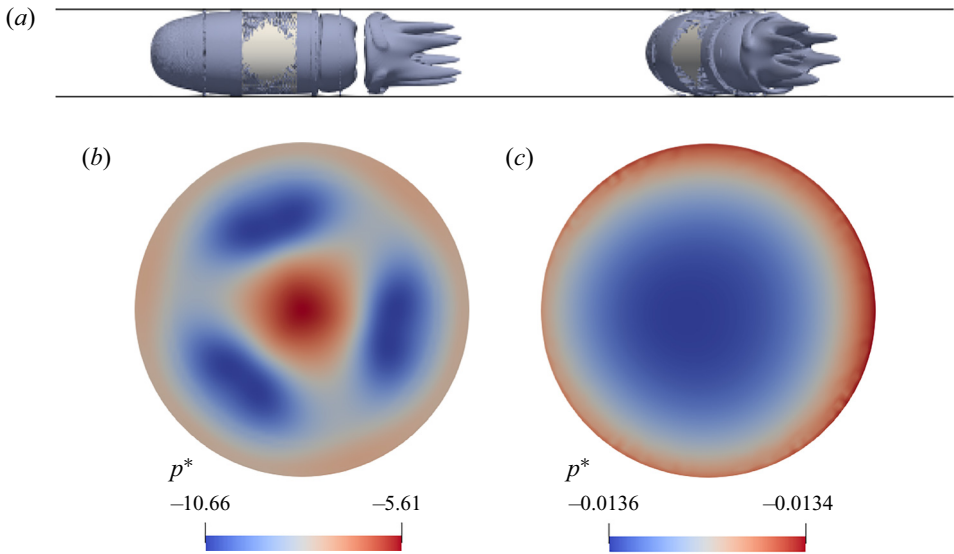


Figure 25. Illustration of the wake for $a/A = 0.85$ and $Re = 150$. Iso-contour of Q-criterion (a), side and rear diagonal views. Slices of the dimensionless pressure $p^* = p/(\rho U^2)$ in the wake of the body, at $x/D = 1.2$ (b) and at $x/D = 9$ (c).

the pressure in a transverse slice just behind the body in figure 25(b) indeed indicates a symmetry of order 3 (i.e. 3 symmetry planes). However, this symmetry is not perfect. Indeed, plotting the pressure in a slice located farther downstream in figure 25(c) rather demonstrates a symmetry of order one because the region of largest pressure (blue levels) is slightly displaced towards the left. The presence of a $m = 1$ component in the flow also manifests by the existence of a non-zero lift force, as indicated by the time series in figure 26. This suggest that the observed flow structure actually results from the presence of both $S1$ and $S3$ modes.

5. Summary and discussion

In this study the stability of the wake induced by a bullet-shaped blunt body moving at constant velocity in moderate and strong confinement conditions has been investigated by the mean of two different numerical approaches. The first one is the global LSA and it has been performed on a rather exhaustive set of parameters (geometrical aspect ratios and Reynolds numbers), more especially the $(a/A, Re)$ plane has been widely explored. One

Flow past a bullet-shaped blunt body in a pipe

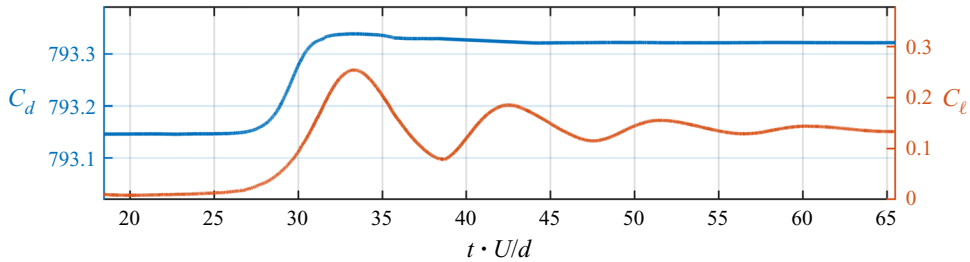


Figure 26. Lift and drag coefficient for DNS case $L/d = 2$, $Re = 150$ and $a/A = 0.85$ vs dimensionless time.

of the main conclusions arising from this first study is that the first destabilization of the axially symmetric is always associated to the stationary mode with azimuthal wavenumber $m = 1$. In the low-confinement regime ($a/A < 0.6$) a sequence similar to the one seen in the unconfined case is observed, characterised by the successive emergence of two stationary ($S1$ and $S2$) modes and two oscillatory modes ($O1$ and $O2$), all with azimuthal wavenumber $m = 1$. Increasing the confinement leads to a decrease of the associated critical Reynolds numbers and an increase of the frequencies of the unsteady mode. The length of the body also influences the results and tends to delay the instability.

On the other hand, in the highly confined regime ($a/A > 0.75$), although the primary mode remains the $S1$ mode, the next ones to emerge are steady modes associated to wavenumbers $m = 2$ and $m = 3$. This range is also associated to a restabilization of most $m = 1$ modes: the oscillating modes $O1$ and $O2$ completely disappear, and the primary stationary mode $S1$ restabilizes, and new unsteady modes called $O3$ and $O4$ characterised by very low frequencies emerge. Interestingly, between these two latter events, there exists a range of Reynolds number where all eigenmodes with $m = 1$ are stable and only unstable modes with $m = 2, 3$ are present. Furthermore, in this high-confinement regime the results become independent upon the length of the body. This is explained by the fact that a parallel flow of Couette–Poiseuille type establishes within the annular gap between the body and the wall.

The second part of this paper is a numerical exploration of the nonlinear dynamics. For this, DNS are performed for various points of the $(a/A, Re)$ plane in order to confront the linear stability findings with numerical experiments. The results of the DNS agrees well with the LSA approach close to the first instability threshold as expected. For low confinement, the bifurcation scenario remains the same as that observed for bullet-shaped blunt bodies. First the loss of axial symmetry occurs through a stationary bifurcation implying a non-zero lift, and then an oscillatory behaviour is exhibited via the RSP state. As the confinement raises, the scenario is no longer valid and other states emerge due to the wall presence. For instance, aperiodic behaviour can be observed for intermediary confinement, $a/A = 0.6$. The nonlinearity effects increase with the confinement as it is illustrated for the RSP state when the section ratio is $a/A = 0.74$. This state differs greatly from the one found for a low confinement: the wake oscillation gathers a large number of harmonics of the same frequency as it has been demonstrated on spectra of the lift and drag coefficients.

We conclude this paper with two last remarks. First, the influence of confinement can be thought of as two ingredients: (i) the effect of the domain restriction by itself and (ii) the effect of an additional shear associated to the boundary layer at the lateral walls. To check their respective influence, we conducted a few tests by replacing the boundary condition at the lateral wall by a ‘slip condition’, hence cancelling the second ingredient. Preliminary

tests considering the case $a/A = 0.75$; $L/d = 2$ lead to contrasted results. On the one hand, the steady $S1$ mode is found to be promoted by a slip condition, with a critical Reynolds detected at $Re_{S1} \approx 63$ compared with 110 with the no-slip condition. On the other hand, an unsteady mode more akin to the $O1$ mode is detected to emerge for $Re_{S1} \approx 200$ with slip condition, in contrast with the fact that this mode vanishes for strong confinement considering no-slip. A complete exploration of this issue is left for future work.

Finally, it is interesting to compare the observation of global instabilities detected by LSA with the prediction of local approaches. Juniper (2006) conducted a comprehensive study of the spatio-temporal stability properties of a family of axisymmetric wake/jets, and identified the ranges of existence of global instabilities as a function of a co-flow parameter $\Lambda^{-1} = (U_1 + U_2)/(U_1 - U_2)$, where U_1 and U_2 are the characteristic velocities of the central and peripheral zones, and of a confinement parameter h which in our case can be identified with $D/d - 1$. Our own results for the base flow indicate a co-flow parameter of order $\Lambda^{-1} \approx 0.2$ in the region located in the near wake ($x/d \approx 1$), and the range we have explored corresponds to a confinement parameter in the range $h \in [0.05-10]$. Considering figure 12(d) of the aforementioned paper, the flow is locally absolutely unstable in this whole range. Hence, predictions of local analysis are consistent with the onset of the global mode. However, as already identified in Bohorquez *et al.* (2011), spatio-temporal local analysis only predicts oscillating modes with non-zero λ_i , so it may only explain the onset of oscillating modes such as $O1, O2, \dots$, but not the steady $S1$ mode which is always the first to emerge.

Acknowledgements. Thanks to ISAE and to HTT teams for the valuable discussions. Computations have been conducted in the CALMIP center, grant no. P20037. The anonymous reviewers are acknowledged for their interesting comments.

Funding. The authors acknowledge the support of Région occitanie under the project ‘HTT Analyse Aéro - Readynov Aero’ number 18012298 under the program FEDER-FSE Midi-Pyrénées and Garonne 2014-2020.

Declaration of interests. The authors report no conflict of interest.

Author ORCIDs.

David Fabre <https://orcid.org/0000-0003-1875-6386>;

Christophe Airiau <https://orcid.org/0000-0001-7453-2964>.

Appendix A. Annular Couette–Poiseuille flow

For strongly confined cases, the flow may be approximated by a parallel flow $\mathbf{u} = u_x(r)\mathbf{e}_x$. With these assumptions the Navier–Stokes equations written in the body frame can be reduced to

$$\frac{1}{r} \frac{\partial}{\partial r} \left(r \frac{\partial u_x}{\partial r} \right) = \mu \frac{dp}{dx}, \tag{A1}$$

where the axial pressure gradient can be shown to be constant. The volume flow rate is given from the product of the front section of diameter D and of the body velocity, i.e. the external wall velocity u_w in the body frame. Let us use, for convenience, the aspect ratio $\xi = d/D$, which is lower than 1. The reference length and reference velocity are respectively set to $d/2$ and u_w . The non-dimensional analytical solution (referred to now as u_x) is easily found by integration, with the help of the no-slip velocity on walls ($u_x(1) = 0$, $u_x(1/\xi) = 1$) and of the conservation of the volume flow rate $q_v = \xi^{-2}u_w\pi d^2/4$.

The solution reads as

$$u_x(r) = \frac{\xi^2(\eta^2 - 1) - (1 + \xi^2) \log \eta}{(1 + \xi^2) \log \xi + 1 - \xi^2}, \quad \eta = \frac{2r}{d}, \quad 1 \leq \eta \leq 1/\xi. \quad (\text{A2})$$

In addition the non-dimensional pressure gradient and the Reynolds number $Re_{d/2}$ are related to ξ by

$$\frac{\xi^2}{(1 + \xi^2) \log \xi + 1 - \xi^2} = \frac{1}{4Re_{d/2}} \frac{dp}{dx}. \quad (\text{A3})$$

Obviously we can see that $Re_{d/2} = Re/2$.

Appendix B. Mesh convergence for DNS simulations

Mesh convergences have been verified to trust the OpenFoam simulations. The output parameters of the convergence analysis are some global quantities as the time average and variance of respectively the drag coefficient ($\overline{C_d}$, σ_{C_d}) and the lift coefficient ($\overline{C_\ell}$, σ_{C_ℓ}). The last output quantity is a Strouhal number evaluated in the body wake. Three main parameters can qualify the mesh quality and they are described in the following.

The first parameter is the number of cells per blunt body diameter $n_{c/D}$. In this study it is chosen in {17, 35, 40, 70}. The refinement levels of the boundary layer developed along the body, referred to as r_{BL} , chosen in {3, 5} is the second parameter. The last parameter is the resulting number of cells (automatically generated). During the mesh processing, the cells in contact with a solid wall are divided in layers tangentially to this wall to ensure a better capture of the boundary layer. The r_{BL} parameter is simply the number of layers defined by the user.

The lengths of the computational domain have been carefully chosen. The extent of each mesh in the streamwise direction is $82 \times d$. The distance between the inlet and the body nose is set to $20 \times d$ and the distance between the body rear and the outlet is $60 \times d$. The convergence study has been performed for a Reynolds number of $Re = 175$. The parameters and the values of the output quantities are reported in table 3. The mesh referred to as F is the finest one and the results from simulations are considered as the reference. Relative errors to the data of the F mesh case are also added in the table. It can be seen that the values of the drag coefficient $\overline{C_d}$ and of the Strouhal St are converged for all meshes, even for mesh A the coarsest one which could be assumed to be of bad quality. The relative errors are lower than 0.46 % for C_d coefficients and lower than 0.77 for the non-dimensional frequencies St . The lift coefficient C_ℓ can still be considered as converged for all meshes with a maximal relative error up to 2.3 % for mesh A. Nevertheless, it seems to be more difficult to reach convergence for the variances of C_d and C_ℓ . The explanation can be found in the very low level of these variances compared with the mean value of C_d and C_ℓ coefficients. It indicates a very low amplitude of the fluctuations and that numerically some large dense meshes are always required in such a case.

Finally, mesh B (see figure 27) has been selected for the main computations in this paper because it is the best compromise between numerical accuracy, mesh size and computer resources.

The variances are quite low for C_ℓ and C_d , respectively being 6.8 % and 2 %. For Reynolds numbers Re other than 175, the number of cells in the boundary layer has been kept by using the scaling given by the law relative to the laminar boundary layer thickness and the Reynolds number $\delta_{BL}/d \propto Re^{-1/2}$.

Mesh ref.	Cells ($\times 10^6$)	n_c/D	n_{BL}	\overline{C}_d	σ_{C_d}	\overline{C}_ℓ	σ_{C_ℓ}	St
A	0.28	17	5	6.8043 0.46 %	0.013311 30 %	0.26079 2.3 %	0.034502 5.6 %	0.28439 0.77 %
B	1.29	35	3	6.8075 0.42 %	0.010950 6.8 %	0.26237 1.7 %	0.032857 2.0 %	0.28603 0.20 %
C	1.55	35	5	6.8292 0.01 %	0.011845 15 %	0.26390 1.2 %	0.034830 7.0 %	0.28711 0.18 %
D	3.13	40	5	6.8381 0.03 %	0.011418 11 %	0.26505 0.73 %	0.034094 5.8 %	0.28813 0.54 %
E	8.46	70	3	6.8270 0.13 %	0.009906 3.2 %	0.26628 0.27 %	0.031337 2.6 %	0.28617 0.14 %
F	9.50	70	5	6.8381 ref.	0.010255 ref.	0.26700 ref.	0.032210 ref.	0.28659 ref.

Table 3. Comparison of global quantities for different meshes ($Re = 175$, $a/A = 0.39$, $d/D = 0.625$, $L/d = 2$).

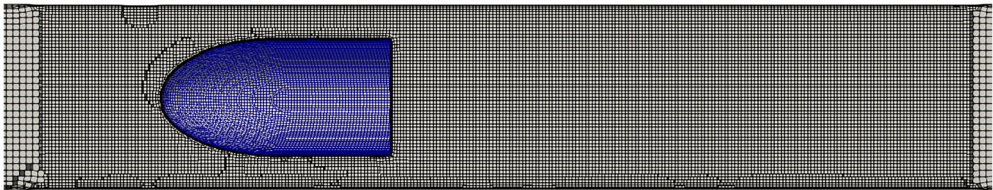


Figure 27. Axial cut-off of the mesh B.

REFERENCES

AUGUSTE, F., FABRE, D. & MAGNAUDET, J. 2010 Bifurcations in the wake of a thick circular disk. *Theor. Comput. Fluid Dyn.* **24** (1–4), 305–313.

BARON, A., MOSSI, M. & SIBILLA, S. 2001 The alleviation of the aerodynamic drag and wave effects of high-speed trains in very long tunnels. *J. Wind Engng Indus. Aerodyn.* **89** (5), 365–401.

BÉNARD, H. 1908 Formation de centres de giration à l’arrière d’un obstacle en mouvement. *C. R. Acad. Sci.* **147**, 839–842.

BOHORQUEZ, P., SANMIGUEL-ROJAS, E., SEVILLA, A., JIMÉNEZ-GONZÁLEZ, J.-I. & MARTÍNEZ-BAZÁN, C. 2011 Stability and dynamics of the laminar wake past a slender blunt-based axisymmetric body. *J. Fluid Mech.* **676** (1), 110–144.

BRAUN, J., SOUSA, J. & PEKARDAN, C. 2017 Aerodynamic design and analysis of the hyperloop. *AIAA J.* **55** (12), 4053–4060.

BRÜCKER, C. 2001 Spatio-temporal reconstruction of vortex dynamics in axisymmetric wakes. *J. Fluids Struct.* **15** (3–4), 543–554.

BURY, Y. & JARDIN, T. 2012 Transitions to chaos in the wake of an axisymmetric bluff body. *Phys. Lett. A* **376** (45), 3219–3222.

CALLAHAM, J.L., RIGAS, G., LOISEAU, J.-C. & BRUNTON, S.L. 2021 An empirical mean-field model of symmetry-breaking in a turbulent wake. Preprint. [arXiv:2105.13990](https://arxiv.org/abs/2105.13990).

CHOI, J.-K. & KIM, K.-H. 2014 Effects of nose shape and tunnel cross-sectional area on aerodynamic drag of train traveling in tunnels. *Tunnel. Underground Space Technol.* **41**, 62–73.

CITRO, V., TCHOUFAG, J., FABRE, D., GIANNETTI, F. & LUCHINI, P. 2016 Linear stability and weakly nonlinear analysis of the flow past rotating spheres. *J. Fluid Mech.* **807**, 62–86.

FABRE, D., AUGUSTE, F. & MAGNAUDET, J. 2008 Bifurcations and symmetry breaking in the wake of axisymmetric bodies. *Phys. Fluids* **20** (5), 051702.

FABRE, D., CITRO, V., FERREIRA SABINO, D., BONNEFIS, P., SIERRA, J., GIANNETTI, F. & PIGOU, M. 2018 A practical review on linear and nonlinear global approaches to flow instabilities. *Appl. Mech. Rev.* **70** (6), 060802.

Flow past a bullet-shaped blunt body in a pipe

- FABRE, D., LONGOBARDI, R., BONNEFIS, P. & LUCHINI, P. 2019 The acoustic impedance of a laminar viscous jet through a thin circular aperture. *J. Fluid Mech.* **864**, 5–44.
- FABRE, D., TCHOUFAG, J., CITRO, V., GIANNETTI, F. & LUCHINI, P. 2017 The flow past a freely rotating sphere. *Theor. Comput. Fluid Dyn.* **31** (5), 475–482.
- HECHT, F. 2012 New development in freefem++. *J. Numer. Math.* **20** (3–4), 251–265.
- JIMÉNEZ-GONZÁLEZ, J.-I., SEVILLA, A., SANMIGUEL-ROJAS, E. & MARTÍNEZ-BAZÁN, C. 2014 Global stability analysis of the axisymmetric wake past a spinning bullet-shaped body. Preprint. [arXiv:1404.0803](https://arxiv.org/abs/1404.0803).
- JUNIPER, M.P. 2006 The effect of confinement on the stability of two-dimensional shear flows. *J. Fluid Mech.* **565**, 171–195.
- KWON, H.-B., KIM, T.-Y., LEE, D.-H. & KIM, M.-S. 2003 Numerical simulation of unsteady compressible flows induced by a high-speed train passing through a tunnel. *Proc. Inst. Mech. Engrs, F: J. Rail Rapid Transit* **217** (2), 111–124.
- MAGNAUDET, J. & MOUGIN, G. 2007 Wake instability of a fixed spheroidal bubble. *J. Fluid Mech.* **572**, 311.
- MELIGA, P., CHOMAZ, J.-M. & SIPP, D. 2009a Global mode interaction and pattern selection in the wake of a disk: a weakly nonlinear expansion. *J. Fluid Mech.* **633**, 159–189.
- MELIGA, P., CHOMAZ, J.-M. & SIPP, D. 2009b Unsteadiness in the wake of disks and spheres: instability, receptivity and control using direct and adjoint global stability analyses. *J. Fluids Struct.* **25** (4), 601–616.
- MOK, J.-K. & YOO, J. 2001 Numerical study on high speed train and tunnel hood interaction. *J. Wind Engng Ind. Aerodyn.* **89** (1), 17–29.
- NATARAJAN, R. & ACRIVOS, A. 1993 The instability of the steady flow past spheres and disks. *J. Fluid Mech.* **254**, 323–344.
- OH, J.-S., KANG, T., HAM, S., LEE, K.-S., JANG, Y.-J., RYOU, H.-S. & RYU, J. 2019 Numerical analysis of aerodynamic characteristics of hyperloop system. *Energies* **12** (3), 518.
- OPGENOORD, M. & CAPLAN, P. 2018 Aerodynamic design of the hyperloop concept. *AIAA J.* **56** (11), 4261–4270.
- PIER, B. 2013 Periodic and quasiperiodic vortex shedding in the wake of a rotating sphere. *J. Fluids Struct.* **41**, 43–50.
- PROVANSAL, M., MATHIS, C. & BOYER, L. 1987 Bénard-von Kármán instability: transient and forced regimes. *J. Fluid Mech.* **182**, 1–22.
- RIGAS, G., MORGANS, A.S., BRACKSTON, R.D. & MORRISON, J.F. 2015 Diffusive dynamics and stochastic models of turbulent axisymmetric wakes. *J. Fluid Mech.* **778**, R2.
- RIGAS, G., MORGANS, A.S. & MORRISON, J.F. 2017 Weakly nonlinear modelling of a forced turbulent axisymmetric wake. *J. Fluid Mech.* **814**, 570–591.
- RIGAS, G., OXLADE, A.R., MORGANS, A.S. & MORRISON, J.F. 2014 Low-dimensional dynamics of a turbulent axisymmetric wake. *J. Fluid Mech.* **755**, R5.
- SIPP, D. & LEBEDEV, A. 2007 Global stability of base and mean flows: a general approach and its applications to cylinder and open cavity flows. *J. Fluid Mech.* **593**, 333–358.
- TCHOUFAG, J., FABRE, D. & MAGNAUDET, J. 2014 Global linear stability analysis of the wake and path of buoyancy-driven disks and thin cylinders. *J. Fluid Mech.* **740**, 278–311.
- THOMPSON, M., HOURIGAN, K. & SHERIDAN, J. 1996 Three-dimensional instabilities in the wake of a circular cylinder. *Exp. Therm. Fluid Sci.* **12** (2), 190–196.
- VON KÁRMÁN, T. 1912 Über den mechanismus des flüssigkeits-und luftwiderstandes. *Phys. Z.* **13**, 49–59.